


Review

Research Progress of Topological Quantum Materials: From First-Order to Higher-Order

Bing Liu *  and Wenjun Zhang

School of Physics and Electronic Information, Weifang University, Weifang 261061, China; w.zhang@wfu.edu.cn

* Correspondence: liubing@wfu.edu.cn

Abstract: The exploration of topologically nontrivial states in condensed matter systems, along with their novel transport properties, has garnered significant research interest. This review aims to provide a comprehensive overview of representative topological phases, starting from the initial proposal of the quantum Hall insulator. We begin with a concise introduction, followed by a detailed examination of first-order topological quantum phases, including gapped and gapless systems, encompassing relevant materials and associated phenomena in experiment. Subsequently, we delve into the realm of exotic higher-order topological quantum phases, examining both theoretical propositions and experimental findings. Moreover, we discuss the mechanisms underlying the emergence of higher-order topology, as well as the challenges involved in experimentally verifying materials exhibiting such properties. Finally, we outline future research directions. This review not only systematically surveys various types of topological quantum states, spanning from first-order to higher-order, but also proposes potential approaches for realizing higher-order topological phases, thereby offering guidance for the detection of related quantum phenomena in experiments.

Keywords: quantum Hall effect; topological insulator; topological semimetal; higher-order topological insulator; higher-order topological semimetal; boundary state



Citation: Liu, B.; Zhang, W. Research Progress of Topological Quantum Materials: From First-Order to Higher-Order. *Symmetry* **2023**, *15*, 1651. <https://doi.org/10.3390/sym15091651>

Academic Editors: Tomohiro Inagaki and Tianjun Li

Received: 15 May 2023

Revised: 3 August 2023

Accepted: 21 August 2023

Published: 26 August 2023



Copyright: © 2023 by the authors. Licensee MDPI, Basel, Switzerland. This article is an open access article distributed under the terms and conditions of the Creative Commons Attribution (CC BY) license (<https://creativecommons.org/licenses/by/4.0/>).

1. Introduction

Topological materials have garnered substantial attention in the field of condensed matter physics over the past decade [1–4]. This is due to their remarkable properties in boundary behavior, such as unidirectional and non-dissipative energy transport, which is protected against backscattering. These unique characteristics have significant applications in spintronics and quantum information sciences. Moreover, in recent years, the study of topological materials has expanded significantly into diverse fields, including optics [5], acoustics [6–11], and mechanics [12,13]. This expansion has opened up new opportunities for controlling and designing the propagation of classical waves.

Topology is a mathematical concept that captures the invariant properties of geometric objects under continuous transformations. Objects belonging to the same topological class can be continuously deformed into one another. This shared characteristic is expressed through topological invariants. Initially, topological properties were applied to describe the distribution states of materials in real space. Afterwards, the concept of topology was extended to momentum space. In this context, if the quantum mechanical wave function of a system can undergo an adiabatic deformation to transform into another wave function, they are considered topologically equivalent. For systems consisting of multiple particles, the simple combination of atomic wave functions yields a topologically trivial result. Therefore, if the wave function of a condensed matter system can be adiabatically transformed into the atomic limit, it is deemed the atomic insulator which is topologically trivial; otherwise, it is regarded as topologically nontrivial.

Numerous reviews on topological materials have been published to date, but most of them primarily concentrate on early-stage first-order topological phases within the realms

of electronic or electromagnetic fields [1–4]. However, these reviews overlook the emerging field of higher-order topological phases. In light of this, the objective of this article is to present a comprehensive examination of topological phases, including both first-order and higher-order phases. The discussion will encompass realistic materials, underlying mechanisms, challenges, and future research directions. It is important to acknowledge that the content of this article is constrained by the authors' interests, expertise, and the article's length, resulting in the regrettable omission of many outstanding works.

2. First-Order Topological Quantum Phase

The quantum Hall system stands out as a pioneering example of a topologically nontrivial condensed matter system, marking the inception of research on topological quantum states. Building upon the quantum Hall effect, subsequent discoveries such as the quantum spin Hall effect, quantum anomalous Hall effect, topological insulators, and topological semimetals have unveiled a plethora of novel physical phenomena.

2.1. Quantum Hall Effect

In the 1980s, von Klitzing et al. [14] conducted a groundbreaking experiment where they measured the boundary conductivity of two-dimensional electronic materials subjected to an external magnetic field. Their discovery revealed that the conductivity σ was an integer multiple of a fundamental quantity, e^2/h , denoted as $\sigma = n_H e^2/h$. Moreover, they observed a remarkable step-like change in conductance as the magnetic field strength increased, demonstrating a precise quantization unaffected by parameters such as boundary defects. This phenomenon, known as the “integer quantum Hall effect” [15], earned von Klitzing the Nobel Prize in Physics in 1985.

To elucidate the underlying physical mechanism of the integer quantum Hall effect, researchers have approached its explanation from various perspectives [16–19]. It is evident that a profound connection exists between the integer quantum Hall effect and the topology. Notably, Thouless et al. [17] provided a theoretical insight into the relationship between conductivity and the bulk state of the system. They derived a mathematical formula for calculating conductivity:

$$\sigma_H = n_H \frac{e^2}{h}, n_H = \frac{1}{2\pi} \sum_i \iint_{FBZ} dk^2 \iint i \left(\frac{\partial \bar{u}^i(\mathbf{k}, \mathbf{r})}{\partial k_1} \frac{\partial u^i(\mathbf{k}, \mathbf{r})}{\partial k_2} - \frac{\partial u^i(\mathbf{k}, \mathbf{r})}{\partial k_1} \frac{\partial \bar{u}^i(\mathbf{k}, \mathbf{r})}{\partial k_2} \right) d\mathbf{r}^2, \quad (1)$$

where the index i represents the band index, $u^i(\mathbf{k}, \mathbf{r})$ represents the Bloch state at wave vector \mathbf{k} for the i -th energy band, and $\bar{u}^i(\mathbf{k}, \mathbf{r})$ denotes the complex conjugate of the Bloch state. The index i spans all energy bands below the Fermi energy level. It has been mathematically proven that n_H is an exact integer known as the TKNN number [17], serving as a topological invariant characterizing the quantum Hall effect. Equation (1) is closely associated with the first Chern class in topology [20], introduced by Shiing-Shen Chern. Consequently, the TKNN numbers are often referred to as Chern numbers [19]. An insulator with a Chern number of zero is classified as a trivial insulator, while a non-zero Chern number designates a Chern insulator. The integral term in Equation (1) corresponds to the Berry curvature, a quantity that describes the intrinsic property of Bloch states within the first Brillouin zone.

It is important to note that the aforementioned topological numbers solely rely on the properties of the bulk states, while the quantum Hall effect manifests as a boundary characteristic of a material. This unique feature is a defining aspect of topological materials, where the bulk properties dictate the conductive behavior at the boundary—a phenomenon known as the bulk-edge correspondence [2,3]. At the interface between two insulators with different Chern numbers, topological boundary states emerge and their number is equal to the difference between the two Chern numbers (Figure 1a). These boundary states enable the unimpeded propagation of electronic waves without interference from defects or impurities. Consequently, a dispersion curve appears within the band gap (Figure 1b). This topological property can be understood in terms of the breaking of time reversal symmetry

by the magnetic field. Electrons can only transport in a single direction and are immune to backward scattering, even in the presence of defects or impurities, and the direction of the topological state reverses only when the direction of the magnetic field is reversed.

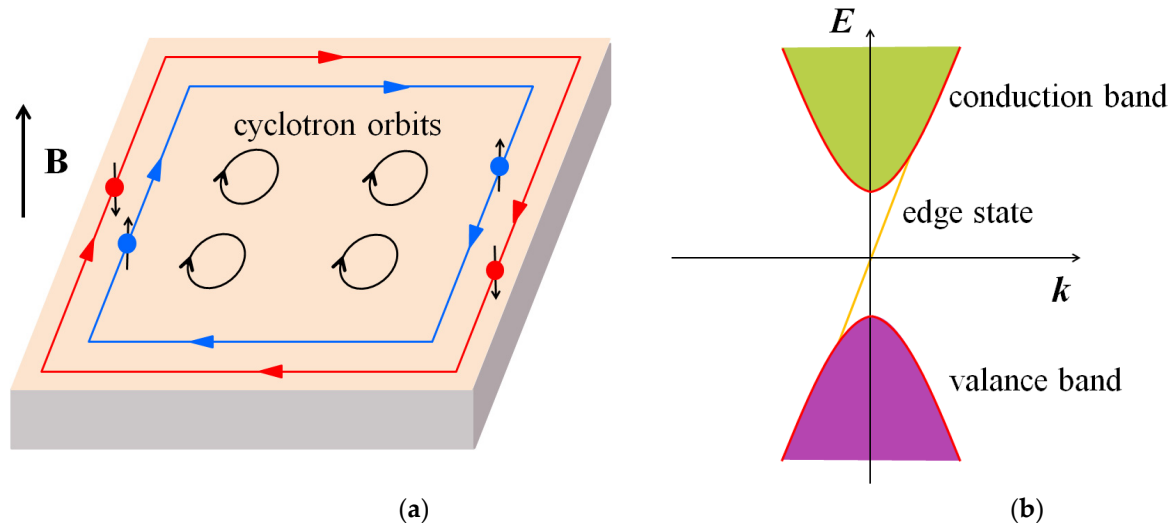


Figure 1. The integer quantum Hall edge state in two-dimensional electronic systems under a strong magnetic field. (a) Spatial image. (b) Energy band image.

2.2. Quantum Spin Hall Effect

The quantum Hall effect is a result of the presence of topologically protected boundary states under an external magnetic field. However, an intriguing question arises: do these non-dissipative boundary states also exist in the absence of an external magnetic field? In 1988, Haldane made a significant breakthrough by recognizing that the key to realizing the quantum Hall effect lies in the breaking of time reversal symmetry. He developed a tight-binding model based on a two-dimensional hexagonal lattice, where each unit cell features a properly positioned magnetic flux [18,21]. Through this model, he derived the corresponding energy band and wave function, leading to the prediction that the quantum Hall conductivity can also be obtained in the absence of a magnetic field. This phenomenon is known as the quantum anomalous Hall effect and is associated with a time-reversal-symmetry breaking topological insulator, also known as the Chern insulator [18,21].

Subsequently, the theoretical conjecture of the quantum Hall effect was further extended to systems with time reversal invariance, wherein the presence of both clockwise and anticlockwise boundary states is expected. Notably, these systems require the inclusion of heavy elements with a significant spin-orbit interaction. The spin-orbit coupling (SOC) plays a crucial role by linking the current direction of the boundary state to the spin direction of the electron. In other words, the spin orientation and orbital motion are locked, giving rise to the phenomenon known as the quantum spin Hall effect.

In a two-dimensional insulator with strong SOC, the SOC acts as an effective spin-dependent magnetic field, giving rise to stable conductive edge states at the material's boundary. Notably, these edge states exhibit a spin-dependent behavior where spin-up electrons travel in one direction while spin-down electrons travel in the opposite direction. This spin-dependent motion leads to the formation of two dispersion curves within the band gap, as depicted in Figure 2. Consequently, there is a net spin transport occurring in the forward and backward directions along the upper and lower boundaries, respectively, equivalent to segregating electrons in the quantum Hall state based on their spins. This remarkable behavior is a characteristic of the quantum spin Hall effect. As long as the time reversal invariance of the system remains unaltered by the absence of a magnetic field or magnetic impurity scatterings, the influence of SOC will continue to dominate the behavior of the topological edge states.

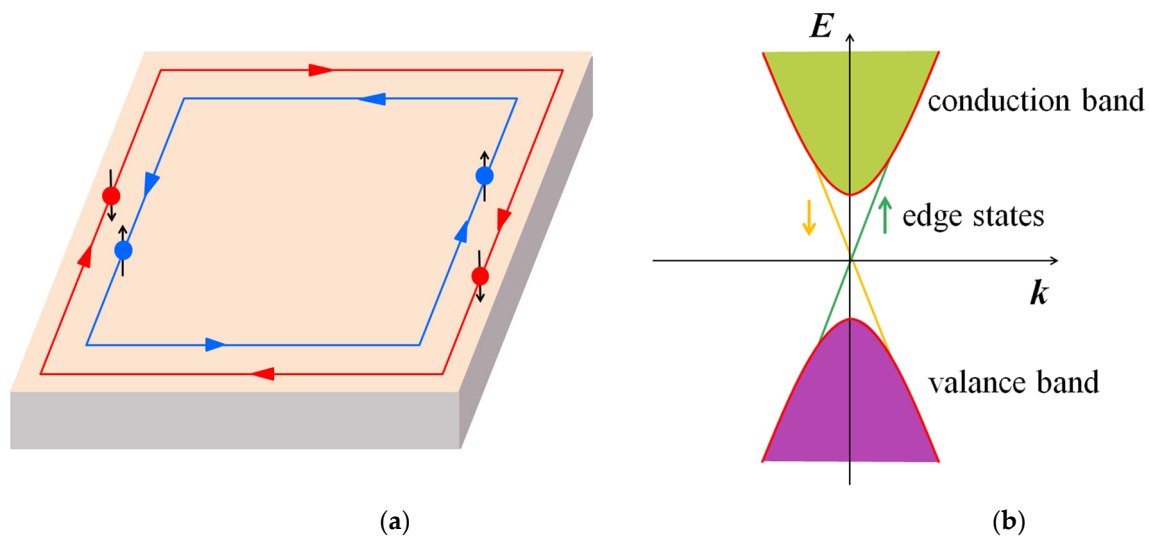


Figure 2. The quantum spin Hall edge states in two-dimensional electronic systems. (a) Spatial image. (b) Energy band image.

A notable example in this context is the extension of the Haldane model to realistic materials. Kane and Mele [22] employed the tight-binding Hamiltonian for the hexagonal lattice to investigate the electronic properties of graphene:

$$H = -t \sum_{\langle ij \rangle \sigma} c_{i\sigma}^{\dagger} c_{j\sigma} + i\lambda_{SO} \sum_{\langle\langle ij \rangle\rangle \sigma \bar{\sigma}} c_{i\sigma}^{\dagger} v_{ij} \mathbf{s}_{\sigma \bar{\sigma}} \cdot \mathbf{z} c_{j\bar{\sigma}} + i\lambda_R \sum_{\langle ij \rangle \sigma \sigma'} c_{i\sigma}^{\dagger} (\mathbf{s}_{\sigma \sigma'} \times \mathbf{d}_{ij}) \cdot \mathbf{z} c_{j\sigma'} + \lambda_v \sum_{i\sigma} \xi_i c_{i\sigma}^{\dagger} c_{i\sigma}, \quad (2)$$

where $c_{i\sigma}^{\dagger}$ and $c_{j\sigma}$ are the creation and annihilation operators acting on lattice sites i and j , respectively. The terms $\langle ij \rangle$ and $\langle\langle ij \rangle\rangle$ represent the summation over nearest neighbors and next nearest neighbors, respectively. The first term accounts for the overlapping of nearest neighbors with an overlapping integral represented by t . The second term incorporates the intrinsic SOC with a strength of λ_{SO} . The third term introduces Rashba SOC, characterized by a strength of λ_R , which breaks the mirror symmetry about the z -axis. The fourth term introduces a staggered sublattice potential that breaks the twofold rotational symmetry within the plane. The strength of the potential on the A (B) sublattice is denoted by λ_v , with $\xi_i = +1(-1)$ representing the onsite energy difference of the A (B) sublattice. Moreover, $v_{ij} = (2/\sqrt{3})(\mathbf{d}_{il} \times \mathbf{d}_{lj})_z = \pm 1$ and \mathbf{d}_{ij} represents the lattice vector pointing from lattice site j to i , and s is the spin Pauli operator. σ and σ' represent the spin index, and $\bar{\sigma} = -\sigma$. This is the Kane-Mele model capturing the quantum phase transition between a quantum spin Hall insulator (a first-order topological insulator) and an ordinary insulator in graphene.

Furthermore, theoretical analyses revealed that the presence of SOC in graphene induced a small gap in the energy spectrum, resulting in an insulating bulk state and spin-dependent conductive states at the material's boundary [22]. Figure 3a displays the energy spectrum of the quantum spin Hall phase observed in zigzag-type graphene nanoribbons, whereas Figure 3b represents the energy spectrum of the trivial phase.

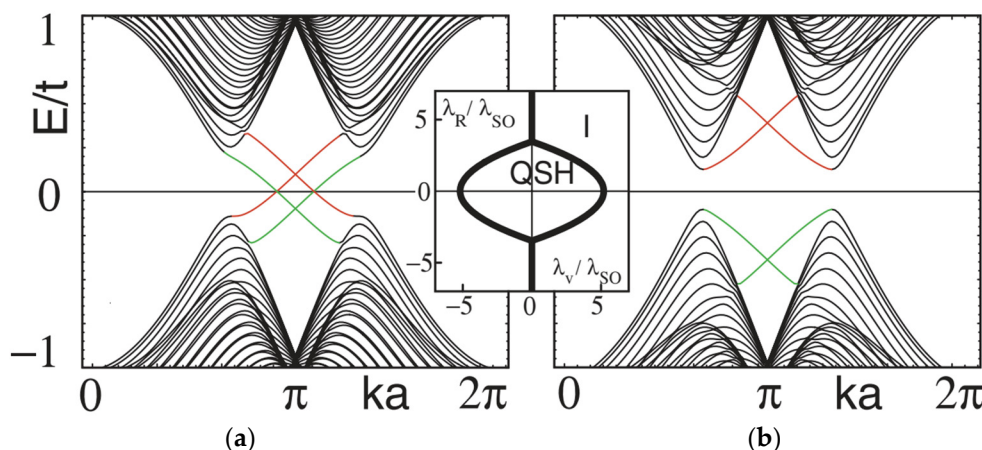


Figure 3. Calculation results for a zigzag-type graphene nanoribbon. (a) The energy spectrum of the quantum spin Hall phase. The edge states appearing in the bulk band gap cross at $ka = \pi$. (b) The energy spectrum of the trivial insulating phase. Reprinted with permission from [22]. Copyright 2005 American Physical Society.

In the quantum spin Hall effect, the edge states with spin-up and spin-down exhibit reversed currents due to time reversal symmetry. As a result, there is no net charge flow, resulting in a Hall conductance of zero. Consequently, the integration of Berry curvature over the Brillouin zone yields a value of zero, making it impossible to characterize the topological properties using the first Chern number. However, upon closer inspection of the two spin subsystems individually, their corresponding Chern numbers are found to be $(1, -1)$, indicating a spin Chern number of 1. Building on this analysis, Kane and Mele [22] introduced a novel Z_2 topological index to describe this spin edge state, distinguishing it from trivial insulating states. Therefore, all two-dimensional insulators that preserve time reversal symmetry can be categorized into two classes based on their Z_2 index: trivial insulators with $Z_2 = 0$ and topological insulators with $Z_2 = 1$.

In order to determine the topological index Z_2 , Kane and Mele [22] introduced a matrix, denoted as $m(k)$, with matrix elements that are given by the expression:

$$m_{ij} = \langle u_i(\mathbf{k}) | T | u_j(\mathbf{k}) \rangle, \tag{3}$$

where $|u_j(\mathbf{k})\rangle$ is the periodic part of the Bloch wave, and i and j range from 1 to N , representing the occupied energy band number. $T = i\sigma_y K$ represents the time reversal operator, in which σ_y is the Pauli matrix and K denotes the complex conjugate. It can be readily shown that $m^T(\mathbf{k}) = -m(\mathbf{k})$ and $m(\mathbf{k})$ is an antisymmetric matrix. In the case of an antisymmetric matrix, we can compute its Pfaffian (Pf) [22]:

$$P(\mathbf{k}) = \text{Pf}[\langle u_i(\mathbf{k}) | T | u_j(\mathbf{k}) \rangle]. \tag{4}$$

On the one hand, if the zeros of $P(\mathbf{k})$ within the Brillouin zone are discrete, the topological index Z_2 is determined by the parity of the number of zeros in half of the Brillouin zone, denoted as B^+ . On the other hand, if the zeros of $P(\mathbf{k})$ are continuous, Z_2 is determined by the parity of half the number of sign changes of $P(\mathbf{k})$ along the boundary of B^+ . These two cases can be expressed in a unified manner as follows:

$$Z_2 = \frac{1}{2\pi i} \oint_{\partial B^+} d\mathbf{k} \cdot \nabla_{\mathbf{k}} \log[P(\mathbf{k} + i\delta)] \text{mod} 2. \tag{5}$$

Kane and Mele’s theoretical research brought significant innovation to the field. However, the practical realization of the quantum spin Hall effect faced challenges due to the weak SOC in carbon, resulting in a small band gap that is susceptible to thermal fluctuations. To overcome this obstacle, Bernevig et al. devised a groundbreaking approach to

investigating topological insulators and the quantum spin Hall effect [23]. They identified HgTe as a material with strong SOC and proposed a semiconductor quantum well structure consisting of a thin layer of HgTe sandwiched between layers of CdTe. Theoretical predictions demonstrated that when the thickness of the HgTe layer exceeds a critical value, a robust quantum spin Hall effect emerges in this two-dimensional system. Subsequently, this effect was experimentally observed in HgTe quantum wells [24]. Notably, the presence of edge states offers a direct means to distinguish a quantum spin Hall insulator from a trivial insulator, as these states manifest as two one-dimensional conducting channels, each contributing a quantized conductivity of e^2/h .

By the way, it is worth noting that the stability of quantum spin Hall insulators relies on the presence of time reversal symmetry. However, in real materials, this symmetry can be easily disrupted by perturbations, which raises concerns about the stability of quantum spin Hall states in real-world environments.

2.3. Quantum Anomalous Hall Effect

The discovery of the quantum spin Hall effect has significantly advanced the exploration of the quantum anomalous Hall effect. By introducing ferromagnetism and breaking the time reversal symmetry, one spin channel in the quantum spin Hall system is suppressed, thereby giving rise to the quantum anomalous Hall effect, as depicted in Figure 4. The quantum anomalous Hall effect offers an alternative avenue to harness the principles of the quantum Hall effect in the absence of an external magnetic field.

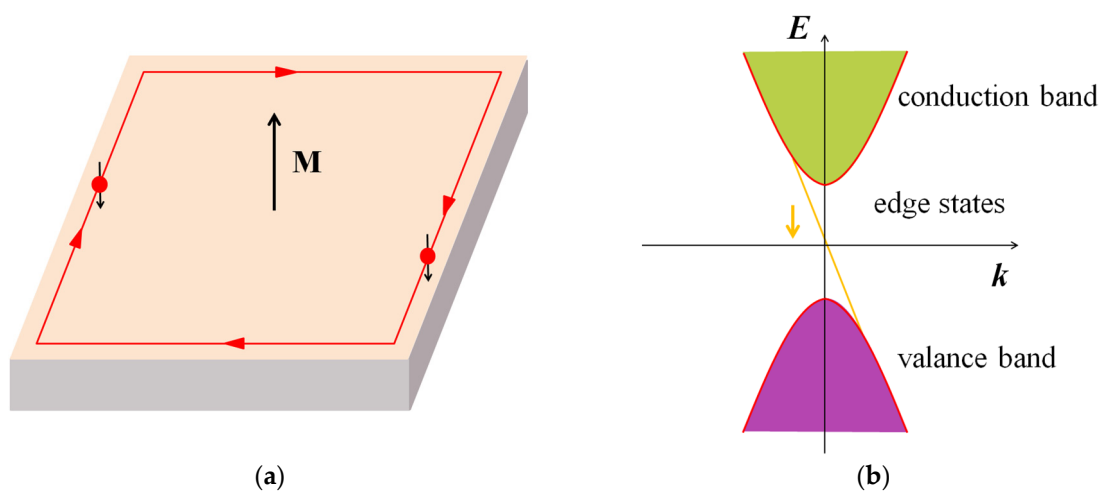


Figure 4. The quantum anomalous Hall edge states in magnetically doped thin films. (a) Spatial image. (b) Energy band image.

The initial breakthrough in the realization of the quantum anomalous Hall effect came from first-principles calculations, which suggested that by thinning and magnetically doping the three-dimensional topological insulator Bi_2Se_3 , it could be possible to achieve this phenomenon [25]. Given the experimental availability of Bi_2Se_3 materials, the introduction of dopants such as Cr or Fe ions in the Bi_2Se_3 thin films was considered. Through the ferromagnetic exchange mechanism between these dopants, the thin films could attain a stable ferromagnetic insulating state with well-defined band gaps and quantized edge states. This makes the doped Bi_2Se_3 system the most promising candidate for realizing the quantum anomalous Hall effect.

Although theoretical predictions suggest the possibility of material realization, practical implementation of the quantum anomalous Hall effect faces challenges due to the presence of electron impurities caused by Se vacancy defects in Bi_2Se_3 . These impurities prevent the strict requirements for achieving the quantum anomalous Hall effect from being met. After years of hard working, Xue's group observed the quantum anomalous Hall

effect experimentally for the first time without the need for an external magnetic field in the magnetically doped thin film of $\text{Cr}_{0.15}(\text{Bi}_{0.1}\text{Sb}_{0.9})_{1.85}\text{Te}_3$ [26]. The Hall conductance exhibits quantization in the region where the longitudinal conductance is zero, as illustrated in Figure 5.

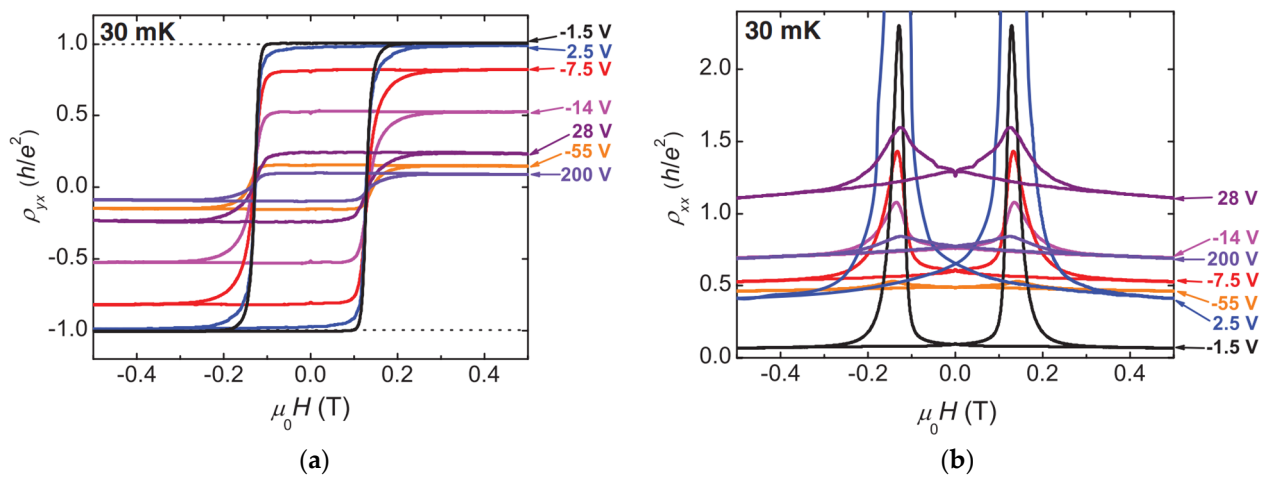


Figure 5. Experimental measurement results of the quantum anomalous Hall effect. The magnetic field dependence of (a) Hall resistivity and (b) longitudinal resistivity at different gate voltages at 30 mK. Reprinted with permission from [26]. Copyright 2013 American Association for the Advancement of Science.

The quantum anomalous Hall effect, quantum Hall effect, and quantum spin Hall effect collectively form a comprehensive trio known as the quantum Hall family [27]. In these three quantized Hall effects, electrons exhibit non-dissipative motion along the material's boundary, while the interior remains insulating. However, there are distinct differences among them. In the quantum Hall effect, electrons of different spins move in a single direction. In the quantum spin Hall effect, electrons of different spins move in opposite directions. In the quantum anomalous Hall effect, only electrons with a spin opposite to the bulk magnetic moment move in a specific direction. The locking mechanism between the spin and the moving direction, as well as the number of edge channels is intrinsic to the material itself.

In the quantum anomalous Hall insulator, the interplay between spontaneous magnetic moment and SOC gives rise to a topologically nontrivial electronic structure, resulting in the emergence of the quantum Hall effect in the absence of an external magnetic field. This unique two-dimensional insulator, also referred to as a Chen insulator, distinguishes itself from ordinary insulators and topological insulators. Its non-zero topological index is determined by the distribution of the Berry curvature of the energy bands in the Brillouin zone [28], similar to the quantum Hall insulator. Additionally, due to the involvement of only one spin channel in conductivity, the non-dissipative conductivity of the quantum anomalous Hall system is less prone to interference compared to the quantum spin Hall system. This characteristic opens up potential applications in low-loss electronic and spintronic devices.

2.4. Three-Dimensional Topological Insulator

Starting from the two-dimensional quantum spin Hall insulator, researchers have explored the generalization of this concept to three-dimensional topological insulators with conductive surface states. The theoretical predictions have been successfully confirmed in practical experiments [29–31]. The surface states of three-dimensional topological insulators exhibit similar characteristics to the Dirac electronic structures observed in graphene, displaying a relativistic linear energy-momentum relationship [29–31]. However, unlike graphene, three-dimensional topological insulators possess only one Dirac cone without

spin degeneracy. To achieve a three-dimensional topological insulator, a strong SOC is required to significantly influence the electronic structure. Therefore, semiconductors containing heavy elements and small band gaps are promising candidates, as the SOC effect is prominent in heavy elements. It is crucial for the band gap to be smaller than the energy scale of SOC to ensure that the transition to a topological insulator occurs.

The first discovered three-dimensional topological insulator is the $\text{Bi}_x\text{Sb}_{1-x}$ alloy [29–31]. Subsequently, the Bi_2Se_3 family, including Bi_2Te_3 and Sb_2Te_3 , with space group D_{3d}^5 ($R\bar{3}m$) was also discovered [32–35]. Compared to the $\text{Bi}_x\text{Sb}_{1-x}$ alloy, the Bi_2Se_3 samples [32,33] are relatively easier to prepare and exhibit topological insulator behavior even at high temperatures, with a band gap larger than 0.1 eV. Notably, the band gap of Bi_2Se_3 is approximately 0.3 eV (equivalent to 3600 K), which greatly exceeds the room temperature energy scale, making it a potential candidate for low-loss spintronic devices at room temperature. First-principles calculations [36] have revealed that the introduction of SOC results in a band inversion at the Γ point, predicting the topological insulator properties of Bi_2Se_3 , Bi_2Te_3 , and Sb_2Te_3 . However, Sb_2Se_3 is considered a trivial insulator due to the weak SOC provided by Sb atoms.

Here, the presence of strong SOC once again plays an important role in the correlation of all the spins of electrons. As illustrated in Figure 6a, at the Fermi level there is only a single spin state along each momentum on the surface, and the spin direction rotates as the momentum moves around the Fermi plane. When disorders or impurities are introduced onto the surface, scattering can occur among the surface states. However, the remarkable feature of topological insulators is that the bulk topological property ensures the persistence of the metallic surface states even in the presence of scattering. In other words, the existence of metallic surface states and their robustness to disorder are fundamental characteristics of three-dimensional topological insulators. Experimental evidence of the Dirac cone for the (111) surface state of Bi_2Se_3 is shown in Figure 6b. It is worth noting that the surfaces of three-dimensional topological insulators do not exhibit complete resistance to backscattering, unlike their two-dimensional counterparts. Even in the absence of magnetic impurities, electrons with the same helical chirality in edge states can still undergo scattering. However, their topological nature guarantees that the metallic behavior does not easily disappear in these systems.

According to the energy band theory of solids, materials can be classified into insulators (including semiconductors) and metals based on their conductivity properties. However, categorization can also be achieved based on the topology of electronic states. Topological insulators, in particular, represent a novel quantum state of matter that is fundamentally distinct from ordinary insulators and metals. In a topological insulator, the bulk exhibits an insulating state with an energy gap, while the surface possesses metallic states without a gap. Unlike typical surface states that arise from unsaturated bonds or surface reconstructions, these metallic surface states are not determined by the specific surface structure but rather by the unique topological characteristics of the bulk wave functions. Importantly, these conductive surface states remain stable based on the premise that certain symmetries (such as time reversal symmetry) are present, and they are resistant to the effects of impurities and disorders. Remarkably, electrons with different spins in a topological insulator move in opposite directions, offering the potential for transmitting information through spin rather than charge.

The three-dimensional strong topological insulator materials Bi_2Se_3 , Bi_2Te_3 , and Sb_2Te_3 are highly desirable for research and experimental investigations due to their ease of growth and handling. These materials serve as ideal platforms for studying and verifying various properties of surface states, including ideal transport without backscattering [37], weak anti-localization effect [38], and more. Furthermore, magnetically doped films of these materials have been utilized to experimentally demonstrate the quantum anomalous Hall effect [39].

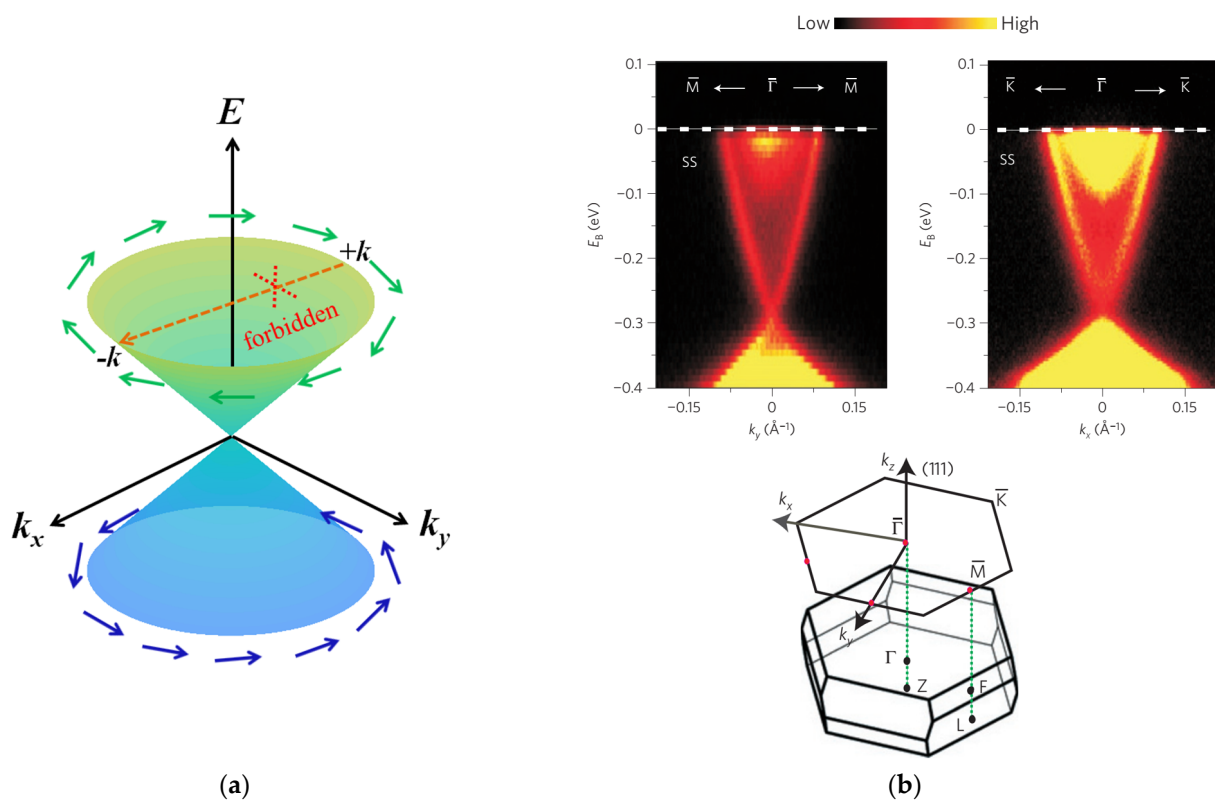


Figure 6. (a) The helical Dirac cone surface states of three-dimensional topological insulators. The green and blue arrows indicate the distribution of electronic spins. (b) The electronic structure of the topological insulator Bi_2Se_3 . The top image shows the band dispersion of the (111) surface measured via angle-resolved photoelectron spectroscopy (ARPES). The bottom image shows the three-dimensional Brillouin zone and the two-dimensional projected Brillouin region for the surface. Reprinted with permission from [33]. Copyright 2009 Nature Publishing Group.

2.5. Topological Semimetal

A topological semimetal is a unique class of material characterized by topologically protected band-crossings near the Fermi level. These band-crossings can occur in different dimensions (point, line, plane) and exhibit various degeneracies (double, quadruple, etc.), resulting in the classification of different types of topological semimetals. Examples include Dirac semimetals [40,41], Weyl semimetals [42–45], double Dirac semimetals [46], nodal line semimetals [47–51], and semimetals with multiple degenerate points [52,53]. Importantly, these topological semimetals exhibit a rich variety of low-energy quasi-particle excitations, providing a platform for studying both solid-state quasi-particles and elemental particles in high-energy physics [53]. Due to their unique bulk and surface properties, topological semimetals display intriguing quantum transport phenomena, such as high mobility and giant magnetoresistance in Dirac semimetals [54,55], negative magnetic resistance and chiral anomalies in Weyl semimetals [56,57]. Furthermore, topological semimetals hold potential applications in diverse fields including chemical catalysis [58,59], quantum computing [60], and spintronics [61].

2.5.1. Dirac Semimetal

In 2004, Novoselov et al. achieved a significant breakthrough by successfully obtaining monolayer graphene through mechanical exfoliation [62]. Graphene, as a prominent example of a Dirac semimetal, exhibits Dirac fermions at the K and K' points in its Brillouin zone, leading to the observation of the quantum Hall effect in experimental studies [63]. More recently, graphene has regained attention due to its exceptional physical properties, including superlattice structures and superconductivity in magic angle graphene [64,65].

Na_3Bi is a notable example of a three-dimensional topological Dirac semimetal, initially predicted by theory [41] and subsequently confirmed by experimental studies [66–69]. It possesses time reversal and threefold rotational symmetry, with two Dirac points along the Γ – A direction. Experimental observations, using techniques such as ARPES [66,67], have revealed the presence of Dirac cones and Fermi arcs connecting the bulk Dirac points, as depicted in Figure 7. Furthermore, transport measurements have demonstrated intriguing phenomena, including negative magnetoresistance attributed to chiral anomalies [68] and quantum oscillation [69]. However, Na_3Bi 's instability and sensitivity to air have posed challenges for further investigations. Another prominent three-dimensional Dirac semimetal, Cd_3As_2 [70], is protected by time reversal and fourfold rotational symmetry, with Dirac points located along the Γ – A direction. This has been confirmed by ARPES experiments [71–73]. In addition, other intriguing phenomena have also been observed in Cd_3As_2 , such as quantum oscillation [74] and negative magnetoresistance arising from chiral anomalies [75,76]. Notably, in 2017, the observation of a three-dimensional quantum Hall effect in Cd_3As_2 nanosheets [77,78] provided a significant breakthrough, expanding the study of the quantum Hall effect beyond two-dimensional systems.

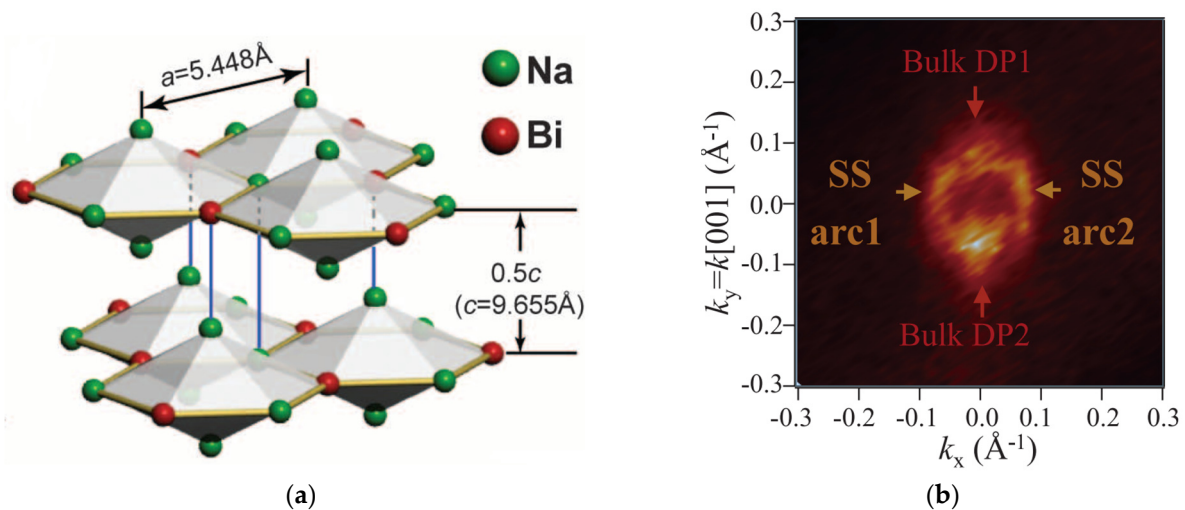


Figure 7. (a) Crystal structure of Na_3Bi . Reprinted with permission from [66]. Copyright 2014 American Association for the Advancement of Science. (b) Fermi surface map of the Na_3Bi sample at photon energy 55 eV. DP1 and DP2 denote the two bulk Dirac points. Reprinted with permission from [67]. Copyright 2015 American Association for the Advancement of Science.

2.5.2. Weyl Semimetal

When either time reversal or spatial inversion symmetry is broken, Dirac semimetals undergo a transition to Weyl semimetals characterized by twofold-degenerate crossings. A key feature of Weyl semimetals is the existence of pairs of chiral fermions, which can be viewed as magnetic monopoles in momentum space. The Weyl fermions with positive and negative chirality, corresponding to Chern numbers of ± 1 , represent the “source” and “leakage” of magnetic monopoles, respectively. Weyl semimetals can be further classified into two categories: the first kind, which obeys Lorentz invariance and exhibits conical Dirac cones near the Fermi energy resembling an “upright” hourglass, exemplified by materials like the TaAs family [43,44,56,57,79–86]; and the second kind, which breaks Lorentz invariance and exhibits tilted Dirac cones, as observed in materials such as WTe_2 [87], MoTe_2 [88–92], MoP_2 [93], and TaIrTe_4 [94]. Fermi arcs and chiral anomalies are considered essential characteristics of Weyl semimetals, and their existence can be verified through ARPES and transport experiments.

TaAs family materials represent the first experimentally confirmed Weyl semimetals [44,80–86]. These materials exhibit twelve pairs of opposite chiral fermions in momentum space and their (001) surfaces have been observed to possess linear dispersion and

Fermi arcs using ARPES techniques [44,80–86], as depicted in Figure 8. Additionally, the transport measurements have revealed the presence of negative magnetoresistance caused by chiral anomalies [56,57,87]. WTe₂, on the other hand, has garnered significant attention as the first predicted type-II Weyl semimetal. ARPES experiments have successfully captured the Fermi arc in WTe₂ [95], while transport studies have demonstrated unsaturated giant magnetoresistance and anisotropic negative magnetoresistance effects [96]. Subsequent experiments have further unveiled intriguing phenomena, including quantum oscillation [97] and the emergence of superconducting states under high pressure [98]. These remarkable characteristics establish WTe₂ as an excellent platform for exploring diverse quantum phenomena.

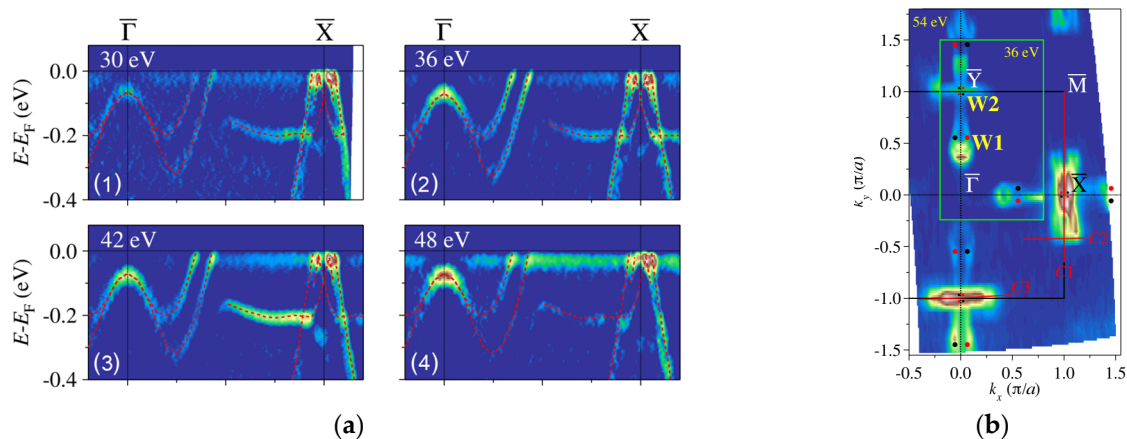


Figure 8. Electronic structure of the (001) surface state in TaAs. (a) Curvature intensity plots of ARPES data. (b) Fermi surface of the TaAs (001) surface, showing the locations of projected Weyl points. Reprinted with permission from [44]. Copyright 2015 American Physical Society.

2.5.3. Nodal Line Semimetal

In 2011, Burkov et al. [99] introduced the concept of nodal line semimetals, emphasizing the additional protection provided by crystal symmetry. Unlike independent points in reciprocal space, band-crossings in nodal line semimetals manifest as continuous lines or rings on the Fermi surface. These crossings can take the form of Dirac points or Weyl points, thereby classifying nodal line semimetals into Dirac nodal line semimetals (e.g., ZrSiS family [100–104]) or Weyl nodal line semimetals (e.g., PbTaSe₂ [105]). Notably, nodal line semimetals exhibit distinctive nontrivial topological surface states known as drumhead-type states, contrasting the Fermi arc surface states observed in Dirac and Weyl semimetals. Furthermore, nodal line semimetals serve as a bridge for the transformation between different topological states. Figure 9 illustrates the relationship between the symmetries and electronic structures of different topological states. By introducing SOC and breaking crystal symmetries, various topological semimetals and topological insulators can be realized based on a spinless Dirac nodal line semimetal [106]. For instance, a spinless Dirac nodal line semimetal can be transformed into a Dirac semimetal by combining time reversal, inversion symmetry, and n -fold rotational symmetry. However, it is important to note that the realization of Dirac semimetals and other topological states is not limited to the method shown in Figure 9.

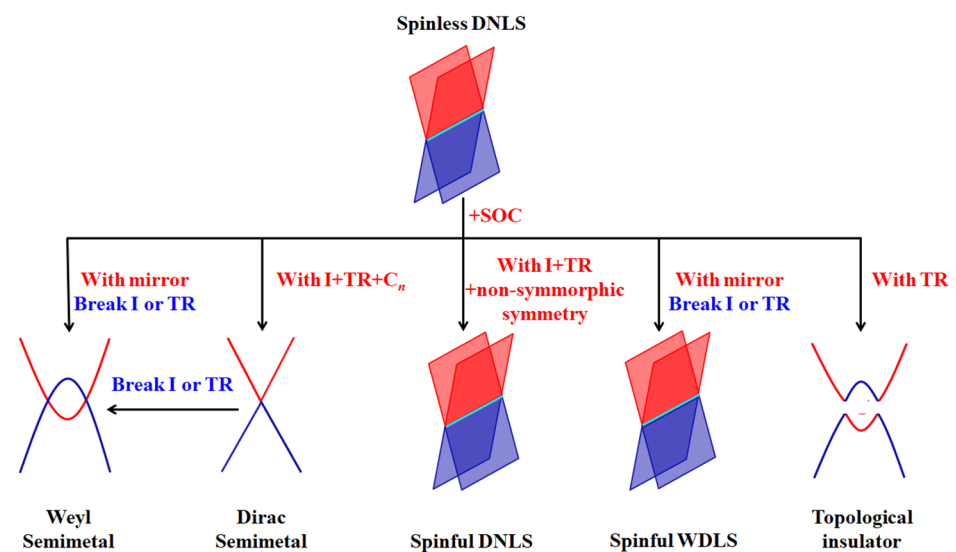


Figure 9. The connections and relationships of topological semimetals.

3. Higher-Order Topological Quantum Phase

The discovery of the quantum Hall insulator marked the beginning of the quest for topologically nontrivial phases in quantum materials. Since then, there has been a growing desire to uncover additional quantum phases exhibiting intriguing topological behaviors and associated fundamental physical properties. As the understanding of topological states advanced, it was discovered that crystal spatial symmetry can provide protection to topological states, giving rise to topological crystalline insulators.

3.1. Topological Crystalline Insulator

In 2009, Kitaev utilized K-theory to derive the topological classification of systems with three internal symmetries: time reversal symmetry, particle-hole symmetry, and chiral symmetry, across various dimensions [107]. Subsequently, Stone, Chiu, and other researchers organized this classification into ten distinct topological classes [108,109], commonly known as the “ten-fold way”, as depicted in Figure 10. However, the topological periodic table solely takes into account the influence of three non-spatial symmetries on the system’s topological classification. In the context of condensed matter physics, this limited consideration of non-spatial symmetries is inadequate for materials with different crystal symmetries. Consequently, the assessment of how crystal space symmetry impacts the system’s topological classification emerges as an urgent issue requiring attention.

In 2011, Fu introduced the concept of topological crystalline insulators [110]. In systems without considering spin, he explored topological crystalline insulators protected by fourfold rotational symmetry C_4 and time reversal symmetry using a tight-binding model. He introduced a new Z_2 invariant based on the C_4 rotational invariants and discovered gapless topological surface states protected by nontrivial Z_2 invariants on the (001) surface while maintaining C_4 symmetry. Further research on topological crystalline insulators revealed that among 230 space groups, there generally exist seven topological invariants related to crystal symmetries, including translation, mirror reflection, glide reflection, rotation, screw rotation, spatial inversion, and S_4 symmetry.

Class	T	C	S	0	δ						
					1	2	3	4	5	6	7
A	0	0	0	\mathbb{Z}	0	\mathbb{Z}	0	\mathbb{Z}	0	\mathbb{Z}	0
AIII	0	0	1	0	\mathbb{Z}	0	\mathbb{Z}	0	\mathbb{Z}	0	\mathbb{Z}
AI	+	0	0	\mathbb{Z}	0	0	0	$2\mathbb{Z}$	0	\mathbb{Z}_2	\mathbb{Z}_2
BDI	+	+	1	\mathbb{Z}_2	\mathbb{Z}	0	0	0	$2\mathbb{Z}$	0	\mathbb{Z}_2
D	0	+	0	\mathbb{Z}_2	\mathbb{Z}_2	\mathbb{Z}	0	0	0	$2\mathbb{Z}$	0
DIII	-	+	1	0	\mathbb{Z}_2	\mathbb{Z}_2	\mathbb{Z}	0	0	0	$2\mathbb{Z}$
AII	-	0	0	$2\mathbb{Z}$	0	\mathbb{Z}_2	\mathbb{Z}_2	\mathbb{Z}	0	0	0
CII	-	-	1	0	$2\mathbb{Z}$	0	\mathbb{Z}_2	\mathbb{Z}_2	\mathbb{Z}	0	0
C	0	-	0	0	0	$2\mathbb{Z}$	0	\mathbb{Z}_2	\mathbb{Z}_2	\mathbb{Z}	0
CI	+	-	1	0	0	0	$2\mathbb{Z}$	0	\mathbb{Z}_2	\mathbb{Z}_2	\mathbb{Z}

Figure 10. Periodic table of topological insulators and superconductors. $\delta: = d - D$, where d is the space dimension and $D + 1$ is the codimension of defects; the leftmost column (A, AIII, . . . , CI) denotes the ten symmetry classes of fermionic Hamiltonians, which are characterized by the presence or absence of time reversal (T), particle-hole (C), and chiral (S) symmetries of different types denoted by ± 1 . Reprinted with permission from [109]. Copyright 2016 American Physical Society.

SnTe is the first topological crystalline insulator material to be theoretically predicted and experimentally verified as protected by mirror symmetry [111]. It exhibits mirror symmetry in the (001) and (110) directions and features an even number of Dirac cone-like surface states without energy gaps on high-symmetry crystal surfaces, such as {001}, {110}, and {111}. Additionally, members of the same family, such as PbTe and PbSe, can also become topological crystalline insulators when subjected to band inversion under the influence of pressure, strain, or doping. Subsequently, ARPES experiments quickly confirmed the existence of Dirac cone-like surface states protected by mirror symmetry in SnTe and $\text{Pb}_{1-x}\text{Sn}_x\text{Se}$ [112,113].

KHgSb is the second topological crystalline insulator material that was theoretically predicted and experimentally verified to be protected by glide symmetry [114,115]. Its surface exhibits an hourglass-shaped two-dimensional topological surface state protected by non-symmorphic symmetry. For this three-dimensional system with both glide symmetry and time reversal symmetry, a new \mathbb{Z}_2 topological invariant can be defined, in addition to the time-reversal \mathbb{Z}_2 invariant, to characterize the system’s topology [116–118].

In 2019, Fang and Fu made a significant discovery of an anomalous type of topology in two-dimensional systems possessing both time reversal symmetry and C_n rotational symmetry ($n = 2, 4, \text{ and } 6$). Typically, any two-dimensional lattice with time reversal and C_n symmetries should feature $2n$ Dirac cones. However, in this peculiar state, only n massless Dirac fermions are protected by time reversal and C_n [119]. Subsequently, it was discovered that $\text{Ba}_3\text{Cd}_2\text{As}_4$, $\text{Ba}_3\text{Zn}_2\text{As}_4$, and $\text{Ba}_3\text{Cd}_2\text{Sb}_4$ represent a class of topological crystalline insulators exhibiting a C_2 rotational anomaly. These compounds showcase two surface Dirac cones on both upper and lower surfaces perpendicular to the rotation axis. Additionally, $(d - 2)$ -dimensional helical hinge states exist along the edges parallel to the rotation axis, connecting the anomalous Dirac cones on the upper and lower surfaces [120].

In recent years, physicists have advanced the theory of Topological Quantum Chemistry by exploring the connection between band representations and symmetry indicators [121]. This theory enables more precise topological classifications of materials within all 230 space groups, consequently leading to the discovery of a wide range of topological crystalline insulators protected by diverse crystal symmetries [122,123].

Later, researchers discovered that for certain insulators a fully opened energy gap appears on the $(d - 1)$ -dimensional surface, while $(d - 2)$ -dimensional topological boundary

states exist. This type of topological insulator is called a higher-order topological insulator. It is important to note that higher-order topological insulators also rely on the safeguarding of crystal symmetry and can be seen as an extension of topological crystalline insulators. In the following discussion, we will delve into these types of exotic higher-order topological phases: higher-order topological insulators and higher-order topological semimetals.

3.2. Higher-Order Topological Insulator

Topological insulators are known for their remarkable feature of topologically protected boundary states. According to the bulk-edge correspondence [5,124], an m -dimensional topological insulator exhibits $(m-1)$ -dimensional gapless boundary states. However, in 2017, researchers [125,126] introduced a new class of topological insulators that break the bulk-edge correspondence, known as higher-order topological insulators. These unique insulators possess lower-dimensional boundary states. Specifically, an m -dimensional n -order topological insulator features $m-1$, $m-2$, $(m-n+1)$ -dimensional gapped boundary states, and $(m-n)$ -dimensional gapless boundary states. For instance, in a three-dimensional system, a second-order topological insulator displays hinge states, while a third-order topological insulator exhibits corner states. In a two-dimensional system, a second-order topological insulator will showcase zero-dimensional corner states, as illustrated in Figure 11.

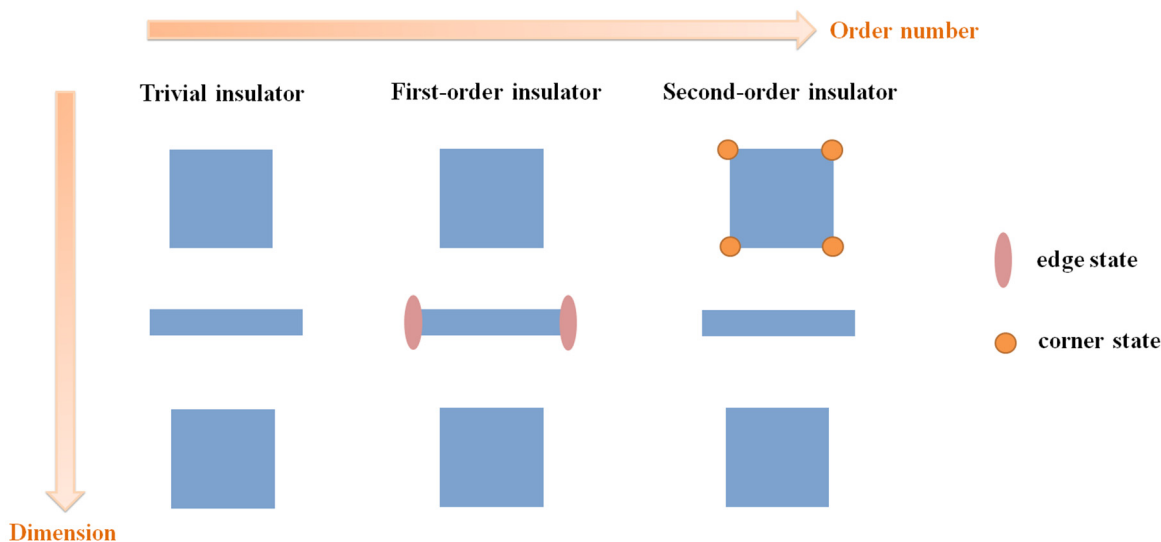


Figure 11. A schematic diagram of the boundary modes of topological matter.

To date, the existence of higher-order topological insulators has been experimentally confirmed in various systems, including mechanical systems [127], microwave systems [128], electrical circuits [129], acoustic systems [130,131], photonic systems [132], and elastic systems [133]. In the following sections, we will introduce three notable models of higher-order topological insulators.

3.2.1. Quantized Quadrupole Topological Insulator

In 2017, Benalcazar, Bernevig, and Hughes introduced the concept of the quantum multipole moment insulator [134,135]. In classical physics, the primitive dipole, quadrupole, and octupole moments of a continuum volume charge density $\rho(\mathbf{r})$ are defined as $p_i = \int d^3\mathbf{r}\rho(\mathbf{r})r_i$, $q_{ij} = \int d^3\mathbf{r}\rho(\mathbf{r})r_i r_j$ and $o_{ijk} = \int d^3\mathbf{r}\rho(\mathbf{r})r_i r_j r_k$, respectively [136]. In the modern theory of polarization in crystals, the dipole moment p_i corresponds to the Berry phase of the bulk electronic states:

$$p_i = \frac{e}{2\pi} \int_{BZ} Tr[A], \tag{6}$$

where BZ indicates the Brillouin zone and the Berry connection A is characterized by components $[A_i(\mathbf{k})]^{mn} = -i\langle u_k^m | \partial_{k_i} | u_k^n \rangle$, where $|u_k^n\rangle$ represents the Bloch function of band n , and the index n is limited to the occupied energy bands. The dipole moment p_i is essentially associated with the presence of surface charge. Benalcazar et al. [134,135] derived the electromagnetic properties of a two-dimensional insulator with a square shape and a three-dimensional insulator with a cubic shape, having only a nonvanishing q_{ij} or o_{ijk} as:

$$\begin{aligned} p_j^{edge\alpha} &= n_i^\alpha q_{ij}, Q^{corner\alpha,\beta} = n_i^\alpha n_j^\beta q_{ij} \\ q_{jk}^{face\alpha} &= n_i^\alpha o_{ijk} \\ p_k^{hinge\alpha,\beta} &= n_i^\alpha n_j^\beta o_{ijk} \\ Q^{corner\alpha,\beta,\gamma} &= n_i^\alpha n_j^\beta n_k^\gamma o_{ijk} \end{aligned} \quad , \quad (7)$$

respectively, where repeated indices are summed over. Here, $p_j^{edge\alpha}$ represents the edge tangential polarizations per unit length on the square, $p_j^{hinge\alpha,\beta}$ represents the hinge tangential polarizations per unit length on the cube, $q_{jk}^{face\alpha}$ represents the surface quadrupoles per unit area of the cube, and $Q^{corner\alpha,\beta}$ and $Q^{corner\alpha,\beta,\gamma}$ are the charges localized on the corners of the square and cube. The Greek letters $\alpha, \beta, \lambda = \pm x, \pm y, \pm z$ label the surfaces of the square/cube, with outward pointing unit normal vectors $n_i^\alpha = s_\alpha \delta_i^{|\alpha|}$ where the sign $s_{\alpha=\pm} = \pm 1$ encodes the direction. These properties are represented pictorially in Figure 12 [134].

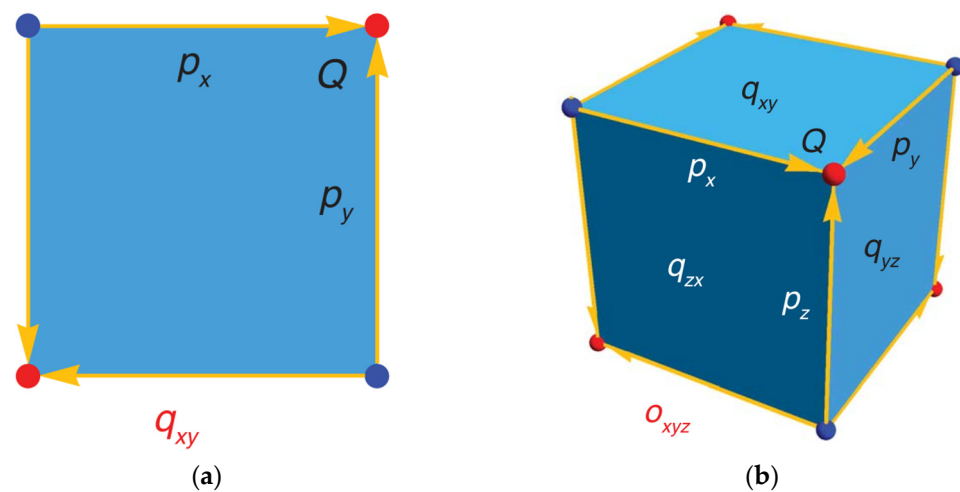


Figure 12. Quadrupole and octupole moments. (a) Bulk quadrupole moment q_{xy} and its boundary polarizations p_i and corner charges Q . (b) Bulk octupole moment o_{xyz} and its surface quadrupoles q_{ij} , hinge polarizations p_i , and corner charges Q . Reprinted with permission from [134]. Copyright 2017 American Association for the Advancement of Science.

However, it is important to note that the values of these moments are not arbitrary, but rather constrained to specific quantized values. Crystal symmetries impose restrictions on these moments [135], requiring that a moment that is odd under a particular symmetry either vanishes or takes on a nontrivial quantized value permitted by the lattice structure. For instance, in a two-band inversion-symmetric insulator at half-filling where there is only one electron per unit cell, the electron center of charge must either coincide with the atomic center ($p_i = 0$) or be positioned halfway between centers ($p_i = \pm e/2$). Any other position of the electron would violate the inversion symmetry, as depicted in Figure 13. As a consequence, the correlation between the multipole moments in Equation (7) leads to the quantization of q_{ij} and o_{ijk} as well.

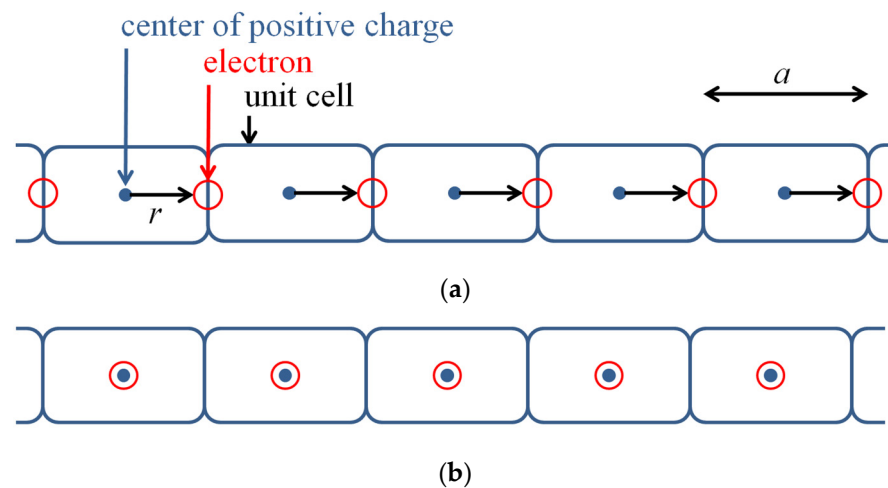


Figure 13. Two one-dimensional lattices with one atomic site (blue dots) and one electron (red circles) per unit cell. The electric dipole moment p_i is $\pm e/2$ in (a) and 0 in (b) due to the difference in the electron center of charge.

Furthermore, it is important to consider that in two-dimensional topological insulators, one-dimensional topological edge states emerge within the bulk energy gap due to the reduction in dimensionality. From a physical perspective, these dimension-reduction-induced topological edge states can be understood through an alternative approach. The quantization of the bulk dipole moment, resulting from specific symmetries, leads to the accumulation of additional charge on the edges, giving rise to the formation of topological edge states [135]. Within this framework, all early stage two-dimensional topological insulators are classified as first-order topological insulators. Expanding upon the theory of dipole moments in crystalline insulators to encompass multipole moments, a new category of insulators, known as quantized electric quadrupole (octupole) insulators or higher-order topological insulators, has been defined. In these systems, all lower-order moments vanish, but the quadrupole (octupole) moment exhibits a non-zero quantized value. Consequently, for electric quadrupole and octupole insulators, there is no longer any additional charge accumulation on the edges or surfaces.

In particular, the realization of multipole moment topological insulators can be achieved by incorporating positive and negative couplings into a tight-binding model. For instance, in the case of a two-dimensional quadrupole topological insulator, its tight-binding Hamiltonian can be described as follows:

$$H(\mathbf{k}) = [\gamma + \lambda \cos k_x]\Gamma_4 + \lambda \sin k_x\Gamma_3 + [\gamma + \lambda \cos k_y]\Gamma_2 + \lambda \sin k_y\Gamma_1, \quad (8)$$

where $\{\Gamma_\alpha\}$ represents the direct product of the Pauli matrix σ_i and κ_i , satisfying $\Gamma_i = -\sigma_2\kappa_i$ ($i = 1, 2, 3$) and $\Gamma_4 = -\sigma_1\kappa_0$. The model is depicted in Figure 14a, where spinless electrons on a square lattice possess π -phase fluxes in both the x and y directions. Figure 14b illustrates the spectral function of γ/λ for an open boundary system, where the red flat band corresponds to the presence of four degenerate corner states, as shown in the right panel.

Subsequently, several research teams have successfully realized quadrupole moment higher-order topological insulators in various experimental systems. These include microwave circuits [128], phononic systems [129], and photonic systems [137], among others. For instance, in the case of photonic systems, Mittal et al. demonstrated the existence of a quantized quadrupole topological phase on the silicon photon platform, which exhibited zero-dimensional corner states [137]. In their experiment, depicted in Figure 15a, a two-dimensional lattice model composed of nano-photonic silicon ring resonators was used. The unit cell consisted of four ring resonators interconnected by resonators (shown in red and green). By adjusting the coupling strength and symbols via the manipulation of the band gap sizes of the lattice resonant ring and connecting resonant ring, a quantized

bulk quadrupole moment was achieved, resulting in quantized dipole moments along the edge and quantized charges at the corners. When the coupling strength between unit cells exceeded that within the unit cells, the system exhibited nontrivial polarization and supported localized corner states within the band gap, as depicted in Figure 15b. Conversely, when the coupling strength was reversed, the system transitioned into a trivial insulator. Notably, these corner states were found to be more robust compared to those observed in topological insulators with zero quadrupole moment, as they exhibited greater resilience to disorder and avoided coupling into the bulk, as shown in Figure 15c. It is worth mentioning that other systems, such as gyromagnetic materials [138] and dielectric structures [139], also hold potential for realizing quadrupole insulators.

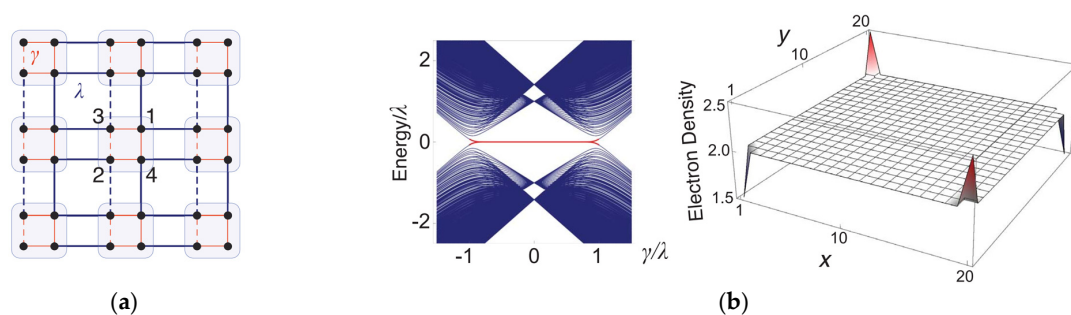


Figure 14. (a) The tight-binding model with a quantized quadrupole moment q_{xy} . γ and λ represent two hopping strengths and the dashed lines represent hopping terms with negative signs. (b) The energy spectrum as a function of γ/λ for a system with open boundary conditions in the x and y directions and the electron charge density distribution in the nontrivial phase. Reprinted with permission from [134]. Copyright 2019 Nature Publishing Group.

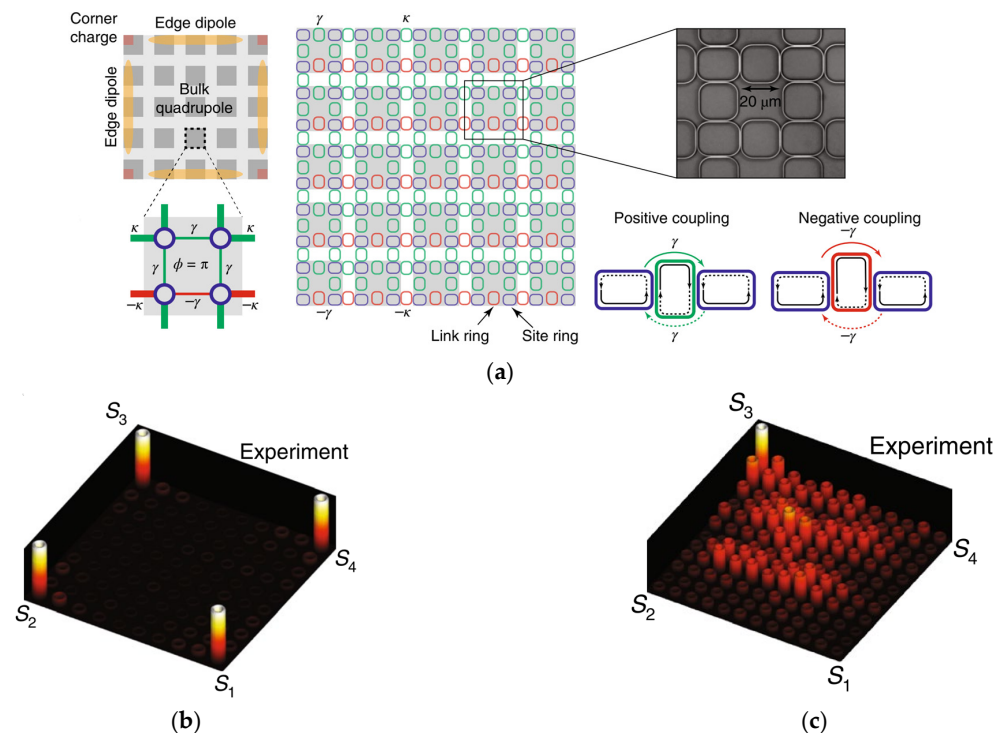


Figure 15. (a) Schematic of the photonic quadrupole topological system composed of ring resonators. (b) In the case of a non-zero quantized quadrupole moment, the measured spatial intensity profile shows the localized corner modes. (c) In the case of a zero quantized quadrupole moment, the measured spatial intensity profile shows the corner modes coupled into the bulk modes. Reprinted with permission from [137]. Copyright 2019 Nature Publishing Group.

3.2.2. Two-Dimensional Su–Schrieffer–Heeger (SSH) Model

The two-dimensional SSH model [140] provides another approach to realizing higher-order topological insulators. In contrast to the previous quadrupole higher-order topological insulator model that requires positive and negative couplings, the two-dimensional SSH model is simpler in its construction. The emergence of corner states in this higher-order SSH model can be attributed to dipole polarization, which describes the displacement of the average position of the Wannier center relative to the unit cell center [130]. The nontrivial two-dimensional SSH phase can be characterized by the two-dimensional Zak phase [141] and the bulk polarization can be defined as follows [142]:

$$P_i = \frac{1}{S} \int_{BZ} A_i(\mathbf{k}) d^2\mathbf{k}, i = x, y. \quad (9)$$

where S is the area of the first Brillouin zone and $A_i(\mathbf{k}) = i\langle \psi_m(\mathbf{k}) | \partial_{k_i} | \psi_n(\mathbf{k}) \rangle$ is the Berry connection. The indices m and n signify the energy bands. Taking the photonic system as an example, Xie et al. initially simulated the presence of local corner states and one-dimensional boundary states in a two-dimensional square lattice [143]. Subsequently, two separate research groups experimentally observed zero-dimensional corner states in the microwave frequency band using near-field scanning techniques. These observations were obtained in a square lattice consisting of dielectric cylinders [144,145]. By controlling the coupling strength both inside and outside the unit cells through adjusting the distances between the medium, the system exhibited a nontrivial phase with a polarization of $(1/2, 1/2)$ when the inter-unit cell coupling strength exceeded the intra-unit cell coupling strength. Conversely, the system transitioned into a trivial phase with a polarization of $(0, 0)$ when the inter-unit cell coupling strength was smaller.

In addition to square lattices, higher-order topological insulators can also be realized in Kagome lattices [142,146]. Figure 16a illustrates a second-order topological insulator configuration in a Kagome lattice [147]. When the inter-unit cell coupling exceeds the intra-unit cell coupling, the bulk polarization becomes $(1/3, 1/3)$, indicating a displacement of the Wannier center from the unit cell center and establishing a nontrivial system characterized by edge states and corner states at the boundary. It is worth noting that in photonic crystals, a new type of higher-order topological phase emerges when considering far-field interactions between non-nearest-neighbor unit cells, which differs from the effects of tight-binding interactions. Experimental measurements of the density of states reveal two types of corner states, as shown in Figure 16b: one arising from bulk polarization (Figure 16c) and the other resulting from far-field interactions (Figure 16d). Furthermore, El Hassan et al. successfully demonstrated local corner states in the visible band using a Kagome lattice constructed with coupled waveguides [148].

3.2.3. Three-Dimensional Higher-Order Topological Insulator

In 2017, Schindler et al. achieved a breakthrough in the field by introducing mass terms that disrupt the original symmetry in first-order topological insulators, leading to the discovery of a three-dimensional higher-order topological insulator [126]. The introduction of these additional mass terms creates effective mass domain walls at the corners or edges of the system, giving rise to the emergence of corner and hinge states [126].

The Hamiltonian of the original two-dimensional topological insulator is expressed as:

$$H(\mathbf{k}) = \left(M + t \sum_i \cos k_i \right) \tau_z \sigma_0 + \Delta_1 \sum_i \sin k_i \tau_x \sigma_i, \quad (10)$$

where $i = x, y$. By introducing an additional mass term, denoted as $H_{mass} = \Delta_2 (\cos k_x - \cos k_y) \tau_y \sigma_0$, which breaks both time reversal symmetry (T) and fourfold rotational symmetry (C_4) while preserving the C_4T symmetry, a higher-order topological insulator with chiral one-dimensional gapless hinge states can be achieved. This is illustrated in Figure 17.

Additionally, Langbehn et al. [149] proposed a three-dimensional second-order topological insulator with broken time reversal symmetry.

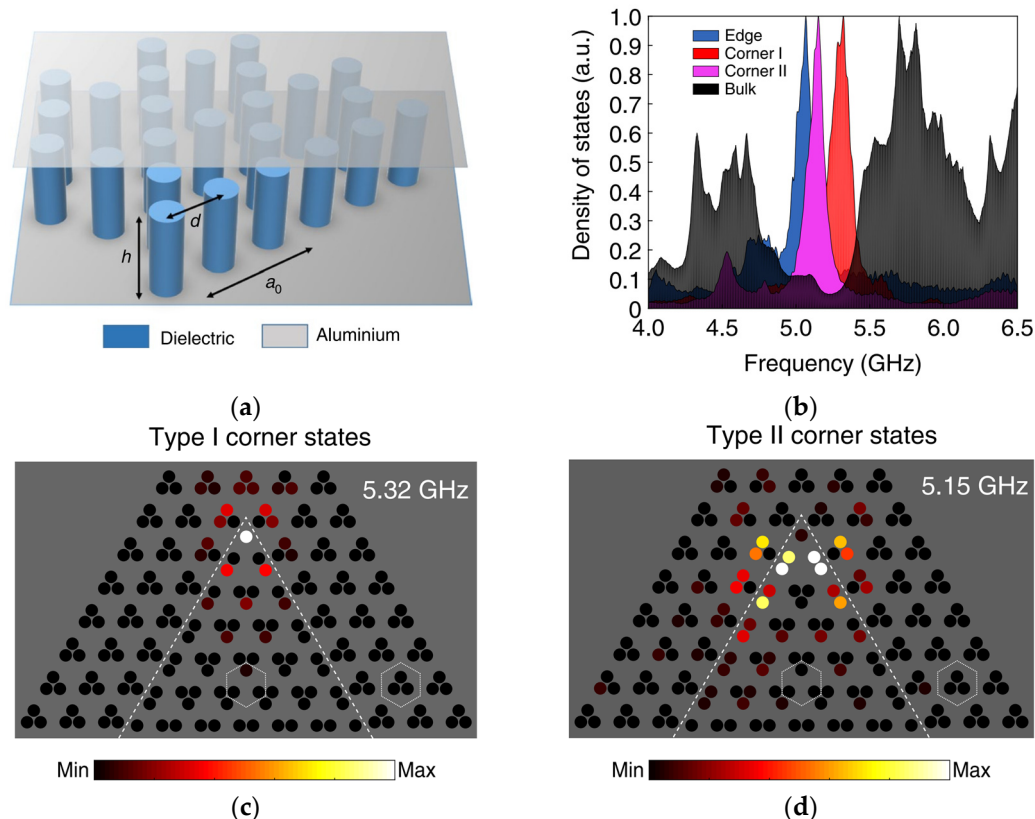


Figure 16. (a) Schematic diagram of the photonic crystal structure with a Kagome lattice. (b) Experimentally measured density of states. (c) Type I corner state. (d) Type II corner state. Reprinted with permission from [147]. Copyright 2020 Nature Publishing Group.

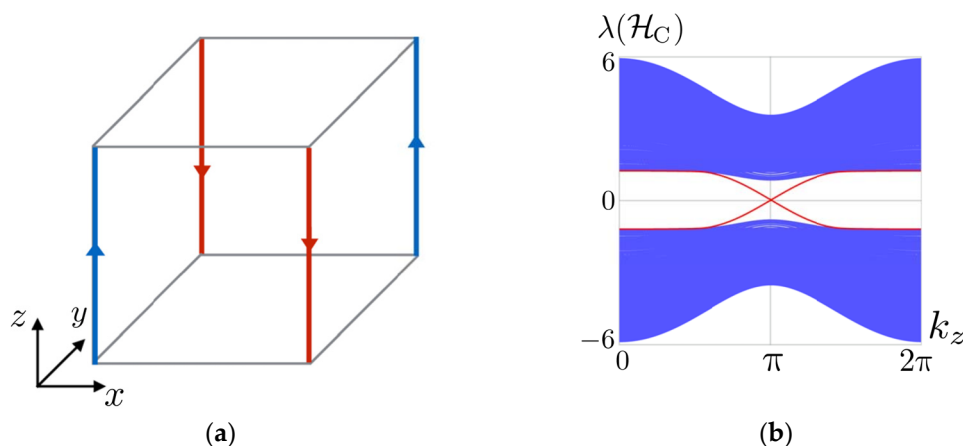


Figure 17. (a) Hinge states of the three-dimensional second-order topological insulator with broken time reversal symmetry. The red and blue arrows indicate chiral hinge currents with inverse directions. (b) The energy spectrum of the three-dimensional chiral higher-order topological insulator, where red lines are the spectrum of hinge states. Reprinted with permission from [126]. Copyright 2018 American Association for the Advancement of Science.

So far, extensive calculations have identified a range of materials that are predicted to exhibit the higher-order topological insulating phase. These include three-dimensional materials such as bismuth [150], transition metal disulfides XTe_2 ($X = Mo, W$) [151], and

shaft insulators like $\text{Bi}_{2-x}\text{Sm}_x\text{Se}_3$ [152] and EuIn_2As [153]. Additionally, two-dimensional materials like twisted bilayer graphene [154,155], graphdiyne [156–158], graphyne [159], monolayer FeSe [160], and covalent organic frameworks [161] have also been considered. Notably, in 2022, our research group made a significant discovery regarding the unique coexistence of topological electron and phonon behavior in graphdiyne [138].

Higher-order topological insulators offer a promising research platform for exploring topologically protected local states with numerous potential applications. For instance, in the field of photonics, the utilization of topological corner modes has shown promise in high-quality and low-threshold lasers [162,163], thereby enabling the development of compact laser devices. Additionally, the concept of surface wave photonic crystals with wide band gaps [164] holds potential for advancements in integrated photonics. Furthermore, in the realm of non-Hermitian systems, the coupling of cavities opens up possibilities for realizing higher-order topological insulators that differ from those found in condensed matter systems [165,166].

3.3. Higher-Order Topological Semimetal

Naturally, the concept of “higher-order” also applies to topological semimetals. In contrast to early stage first-order topological semimetals, higher-order topological phases exhibit lower-dimensional topological boundary states [142,167–171]. For instance, three-dimensional higher-order topological semimetals can possess hinge Fermi arcs or zero-dimensional corner states, while two-dimensional higher-order topological semimetals may exhibit zero-dimensional corner states [167]. As an example, we consider a three-dimensional higher-order semimetal called a quadrupole semimetal, formed by stacking two-dimensional quantum quadrupole moment insulators. The bulk energy band of this system features nodes, while its surface hosts one-dimensional gapless hinge Fermi arcs that connect the projections of the bulk nodes, as illustrated in Figure 18a.

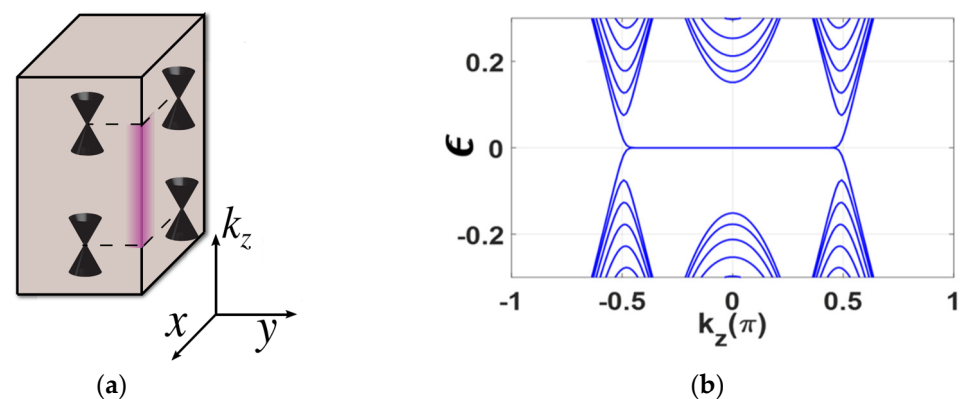


Figure 18. (a) Schematic diagram of the hinge Fermi arc of the three-dimensional quadrupole moment semimetal. Reprinted with permission from [172]. Copyright 2018 American Physical Society. (b) The k_z -dependent energy spectrum of the system with open boundaries in both the x and y directions. Reprinted with permission from [173]. Copyright 2020 American Physical Society.

The Hamiltonian of the three-dimensional quadrupole semimetal can be obtained by parameterizing k_z in Equation (8) [173]:

$$H(\mathbf{k}) = \left[\gamma_x + \frac{1}{2} \cos k_z + \cos k_x \right] \Gamma_4 + \sin k_x \Gamma_3 + \left[\gamma_y + \frac{1}{2} \cos k_z + \cos k_y \right] \Gamma_2 + \sin k_y \Gamma_1. \quad (11)$$

The parameter $\gamma_{x,y}$ represents the intra-unit cell coupling along the x and y directions. In Figure 18b, the k_z -dependent energy spectrum of the system with open boundaries in both the x and y directions is shown. It reveals a fourfold-degenerate zero-energy flat band that terminates at the nodes. This confirms the presence of hinge Fermi arc states

connecting the projection of bulk Dirac points. Therefore, the system exhibits second-order topologically nontrivial boundary states characteristic of a higher-order topological semimetal.

In recent years, it has been discovered that some nodal line semimetals may also exhibit higher-order topology [174–176]. In 2020, Wang et al. [176] proposed a novel second-order nodal line semimetal phase with spacetime inversion symmetry (PT) protection. This phase features a pair of nodal rings and is constructed by stacking two-dimensional second-order Chern insulators with off-diagonal corner states along the k_z direction. Unlike previously known topological semimetal phases that possess protected states only at fixed-order boundaries, this new topological phase exhibits topological states both at the surface and at the hinge regions, as depicted in Figure 19. This unique behavior arises from the bulk of the material being protected by two nontrivial topological charges, namely the real Chern number v_R (also called the second Stiefel-Whitney number [177,178]) and the one-dimensional winding number ω . The definitions of these charges are provided as follows.

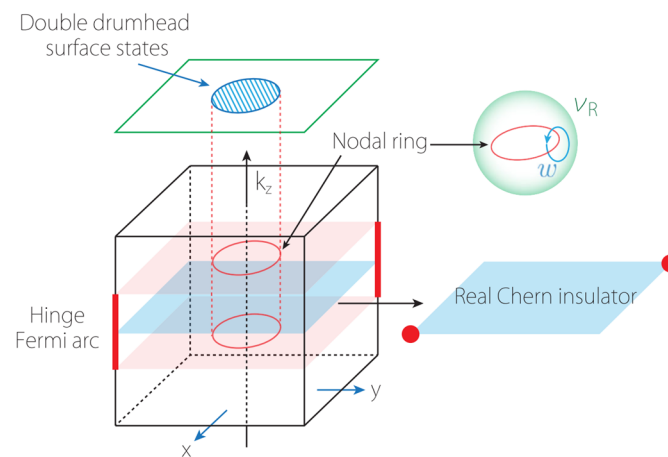


Figure 19. Phase schematic diagram of the second-order nodal line semimetal. Reprinted with permission from [174]. Copyright 2022 American Physical Society.

Firstly, the Z_2 -valued real Chern number v_R is defined as a horizontal two-dimensional plane parallel to the concerned nodal ring. It can be determined by extracting the parity eigenvalues at time reversal invariant momentum points on this plane and then using the following equation [179,180]:

$$(-1)^{v_R} = \prod_i (-1)^{[n_-^{\Gamma_i}/2]}, \quad (12)$$

where $[..]$ denotes the floor function and $n_-^{\Gamma_i}$ represents the number of occupied bands with a negative parity eigenvalue at the time reversal invariant momentum point Γ_i . To confirm the topological nature of a nodal ring, it is necessary to evaluate the real Chern numbers for horizontal two-dimensional planes on both sides of the nodal ring. Physically, if v_R is nontrivial ($v_R = 1$) for one plane and trivial ($v_R = 0$) for another plane, it indicates a switch in topology along k_z , as depicted in Figure 19. This switch implies the presence of nodal lines between the two planes. Moreover, within a specific k_z region $(-k_R, k_R)$ bounded by two nodal rings, if each plane in the region exhibits a nontrivial $v_R = 1$, i.e., a two-dimensional real Chern insulator, they necessarily possess protected zero modes at a pair of PT -connected corners. Collectively, the corner zero modes from all these nontrivial planes form two hinge Fermi arcs within the three-dimensional system.

Secondly, each nodal ring is associated with a Z_2 -valued topological invariant ω , which corresponds to the quantized π Berry phase:

$$\omega = \frac{1}{\pi} \oint_C \text{Tr} A(\mathbf{k}) \cdot d\mathbf{k} \text{ mod } 2, \quad (13)$$

where A represents the Berry connection for the occupied bands and C denotes a closed path encircling the ring (as depicted by the blue cycle with an arrow in Figure 19). Physically, a nontrivial ω ($\omega = 1$) gives rise to a pair of drumhead surface bands confined within the projected nodal rings. This is in contrast to early stage nodal line semimetals, which typically exhibit a single drumhead surface band.

Overall, the two charges, ν_R and ω , give rise to distinct topological boundary modes at different boundaries. The real Chern number ν_R manifests as a pair of hinge Fermi arcs that connect the projected bulk nodal lines on PT -connected hinges, serving as a fingerprint of the second-order topology. On the other hand, the topological charge ω guarantees the existence of double drumhead surface bands.

In recent years, significant advancements have been made in the experimental realization of higher-order nodal line semimetals. For instance, it has been proposed that materials such as $X\text{Te}_2$ ($X = \text{Mo}, \text{W}$) [151] and three-dimensional ABC-stacked graphene [157,174,177] have the potential to exhibit higher-order nodal line semimetal behavior. However, the experimental realization of higher-order Weyl or Dirac semimetals has, thus far, been limited to acoustic and photonic crystals [168,170,171], with their realization in condensed matter systems still remaining elusive.

The exploration of topological materials has expanded beyond first-order topological states to higher-order topological states, leading to significant advancements in both theoretical understanding and experimental realization. However, the study of higher-order semimetals is still in its early stages, and despite the numerous intriguing phenomena proposed in theory, the discovery of suitable real materials remains limited and challenging.

4. Summary and Discussion

Our work provides a comprehensive overview of the research progress in topological phases. In the introduction, we introduce the concept of topology in condensed matter physics. In Section 2, we discuss various early stage first-order topological phases in detail, starting with the quantum Hall insulator as a pioneering example, followed by the quantum spin Hall insulator, quantum anomalous Hall insulator, and topological semimetal. Moving on to Section 3, we provide an exhaustive overview of two intriguing higher-order topological phases.

At present, the hotspot of research on higher-order topological insulators lies in the exploration of new types of topological materials to enrich the family of higher-order topological phases. However, progress in related experimental studies has been slow due to several reasons. Firstly, a relatively limited number of materials have been predicted. While two-dimensional higher-order topological electronic states have been confirmed in certain models such as the square lattice [134,135], Kagome lattice, and honeycomb lattice [130–133], these models have stringent requirements on materials, often limited to a few carbon-based materials, while others are mostly artificial systems. Moreover, there have been few reports on theoretical models related to three-dimensional higher-order topological insulators. Secondly, the growth of electronic materials and the determination of their topological properties still pose challenges in experimental settings. Lastly, current research on higher-order topological insulators mainly focuses on electronic materials, with a lack of exploration in the realm of phononic materials. These unfavorable factors impede further progress in the fundamental theory and experimental investigation of higher-order topological insulators.

Currently, there are only four proposed mechanisms in theory for the formation of higher-order topological insulators in electronic systems. These mechanisms are as follows: (1) the breathing lattice mechanism. This mechanism involves modifying hopping terms

in high-symmetry lattices to induce a “shrinking and swelling” pattern. The reduction in symmetry leads to the lifting of degeneracy of the Dirac bands, resulting in nontrivial higher-order topological energy gaps [142,181]. However, this mechanism has mainly been demonstrated experimentally in artificial acoustic, optical, and elastic systems. (2) The double-band inversion mechanism. In this mechanism, two sets of bands with opposite parities are inverted to induce higher-order topological energy gaps [182]. Experimental confirmation of this mechanism has been observed in only a few three-dimensional electronic materials, such as Bi [150], Td-WTe₂ [183], and Bi₄Br₄ [184]. (3) The in-plane Zeeman field mechanism. By applying an in-plane magnetic field to a topological insulator, time reversal or crystal symmetries are broken, inducing the helical Dirac boundary states or surface states to open the higher-order topological energy gaps [153,185–188]. While some magnetic higher-order topological insulators are expected to exhibit this mechanism, experimental confirmation is still lacking. (4) The structure bending mechanism. This mechanism involves bending the planar structure of a two-dimensional topological crystalline insulator to break crystal symmetry and induce the opening of higher-order topological energy gaps. β -Sb monolayers [189] are proposed as materials where this mechanism can be observed, but experimental verification is still needed. Additionally, the research on the formation mechanisms of higher-order topological insulators in phononic systems is still largely unexplored. Therefore, it is crucial to uncover more formation mechanisms of higher-order topological insulators and identify additional material systems to accelerate progress in experimental detection.

In recent years, there has been significant theoretical research on topological states, focusing on the manipulation of electrons and phonons both domestically and internationally. Notable contributions include the following: (1) Noguchi et al. proposed the use of van der Waals stacking to achieve a transition from a trivial phase to a higher-order topological phase. Different stacking arrangements were shown to lead to different topological states in Bi₄Br₄ [184]. (2) Ezawa suggested that stacking two-dimensional weak topological insulators with varying interlayer coupling strengths can realize both strong and weak three-dimensional higher-order topological insulator phases [190]. (3) Hughes et al. constructed a three-dimensional higher-order topological semimetal by stacking two-dimensional quadrupole square lattices [172]. (4) Liu et al. proposed that applying an electric field can break the mirror symmetry along the (001) crystal direction in SnTe thin films, resulting in a gap in the boundary states [191]. (5) Chen et al. suggested that applying in-plane strain can amplify the influence of twist angles on the phononic structure of twisted multilayer graphene, providing an effective means of manipulating the phononic structure [192]. (6) Jiang et al. proposed that applying biaxial strain to monolayer hexagonal boron nitride can effectively adjust the position of the topological phonon band gap [193]. These theoretical studies demonstrate that factors such as stress, electric field, and stacking can effectively control the electronic and phononic structures of topological materials. Consequently, this opens up new avenues for further research on higher-order topological phases. By exploring the possibilities of topological phase transitions through the application of stress, external fields, interlayer coupling, and other external factors, it becomes possible to manipulate the original electronic and phononic structures of the systems.

In addition, while topological physics has been extensively studied in various electronic and phononic systems, the SOC mechanism that is well-known in electronic systems to open first-order topological energy gaps is not applicable to phononic systems due to the absence of SOC for phonons. As a result, there have been no reports of the coexistence of topological electrons and phonons in the same material for a long time. However, a recent breakthrough has been made by the author’s team, who demonstrated the coexistence of higher-order topological electrons and higher-order topological phonons in graphdiyne with a Kekulé lattice [158], providing the first evidence of higher-order topological phononic states in real materials. This novel topological phase, which combines both electronic and phononic degrees of freedom, offers a promising platform for investigating the interplay

between higher-order topological electronic and phononic states. It is worth noting that when localized higher-order topological electronic states and phononic states overlap in space, strong electron-phonon coupling can occur. This coupling is of particular interest in the context of Bardeen-Cooper-Schrieffer (BCS) superconductivity theory, as strong electron-phonon coupling is a key factor in the emergence of superconductivity. Therefore, it is conceivable that higher-order topological insulators exhibiting the coexistence of electronic and phononic states may hold potential for higher-order topological superconductivity. Nevertheless, due to the early stage of research in this field, our understanding of these materials and their formation mechanisms remains limited.

Based on the above discussions, we believe that further investigations can be conducted in the following areas:

- (1) Studying the models of two-dimensional higher-order topological states and exploring suitable material systems. This entails conducting in-depth theoretical analyses and systematic explorations of the underlying physical mechanisms based on lattice models. It is crucial to recognize that the topological properties of electronic and phononic material systems are influenced by distinct factors. In the case of electronic systems, these factors encompass the lattice structure, atomic orbital types, and SOC. Whereas, for phononic systems, the relevant factors include the lattice structure and atomic vibration modes.
- (2) Investigating the control of two-dimensional higher-order topological states through external manipulation. Building upon existing models and discovered real materials for two-dimensional higher-order topological states, studies should be conducted of the influence of various external factors (such as stress, electric field, magnetic field, and stacking) on the electronic and phononic structures. Future works should also study potential higher-order topological phase transitions, analyze the underlying physical mechanisms, and derive applicable rules and guidelines.
- (3) Exploring the novel category of higher-order topological phases that involve the coexistence of electrons and phonons. Studies can utilize the breathing lattice mechanism to explore this new type of higher-order topological phase where electrons and phonons coexist, as well as uncovering the underlying formation mechanism, thereby establishing a platform for investigating the interplay between electronic and phononic higher-order topological states. Additionally, studies should be conducted of the potential for higher-order topological superconductivity within this context.

Author Contributions: Writing—original draft preparation, B.L.; writing—review and editing, B.L. and W.Z. All authors have read and agreed to the published version of the manuscript.

Funding: This research was funded by the National Natural Science Foundation of China under Grant No. 12204356, by the Natural Science Foundation of Shandong Province under Grant No. ZR2022QA024, ZR2022QA085, and by the foundation from Weifang University.

Data Availability Statement: Data are contained within the article.

Conflicts of Interest: The authors declare no conflict of interest.

References

1. Bansil, A.; Lin, H.; Das, T. Colloquium: Topological band theory. *Rev. Mod. Phys.* **2016**, *88*, 21004. [[CrossRef](#)]
2. Hasan, M.Z.; Kane, C.L. Colloquium: Topological insulators. *Rev. Mod. Phys.* **2010**, *82*, 3045. [[CrossRef](#)]
3. Qi, X.; Zhang, S. Topological insulators and superconductors. *Rev. Mod. Phys.* **2011**, *83*, 1057. [[CrossRef](#)]
4. Armitage, N.P.; Mele, E.J.; Vishwanath, A. Weyl and Dirac semimetals in three-dimensional solids. *Rev. Mod. Phys.* **2018**, *90*, 15001. [[CrossRef](#)]
5. Lu, L.; Joannopoulos, J.D.; Soljačić, M. Topological photonics. *Nat. Photonics* **2014**, *8*, 103–829. [[CrossRef](#)]
6. Zhang, X.J.; Xiao, M.; Cheng, Y.; Lu, M.H.; Christensen, J. Topological sound. *Commun. Phys.* **2018**, *1*, 97. [[CrossRef](#)]
7. Yang, Z.; Gao, F.; Shi, X.H.; Lin, X.; Gao, Z.; Chong, Y.; Zhang, B. Topological acoustics. *Phys. Rev. Lett.* **2015**, *114*, 114301. [[CrossRef](#)] [[PubMed](#)]
8. He, C.; Ni, X.; Ge, H.; Sun, X.C.; Chen, Y.B.; Lu, M.H.; Liu, X.P.; Chen, Y.F. Acoustic topological insulator and robust one-way sound transport. *Nat. Phys.* **2016**, *12*, 1124–1129. [[CrossRef](#)]

9. Xiao, M.; Chen, W.J.; He, W.Y.; Chan, C.T. Synthetic gauge flux and Weyl points in acoustic systems. *Nat. Phys.* **2015**, *11*, 920–924. [[CrossRef](#)]
10. Xie, B.Y.; Liu, H.; Cheng, H.; Liu, Z.; Chen, S.; Tian, J. Experimental realization of type-II Weyl points and fermi arcs in phononic crystal. *Phys. Rev. Lett.* **2019**, *122*, 104302. [[CrossRef](#)]
11. Xie, B.Y.; Liu, H.; Cheng, H.; Liu, Z.; Chen, S.; Tian, J. Acoustic topological transport and refraction in a Kekulé Lattice. *Phys. Rev. Appl.* **2019**, *11*, 44086. [[CrossRef](#)]
12. Huber, S.D. Topological mechanics. *Nat. Phys.* **2016**, *12*, 621–623. [[CrossRef](#)]
13. Rocklin, D.Z.; Zhou, S.N.; Sun, K.; Mao, X. Transformable topological mechanical metamaterials. *Nat. Commun.* **2017**, *8*, 14201. [[CrossRef](#)] [[PubMed](#)]
14. Klitzing, K.V.; Dorda, G.; Pepper, M. New method for high-accuracy determination of the fine-structure constant based on quantized Hall resistance. *Phys. Rev. Lett.* **1980**, *45*, 494–497. [[CrossRef](#)]
15. Cage, M.E.; Klitzing, K.; Chang, A.M.; Duncan, F.; Haldane, M.; Laughlin, R.B.; Pruisken, A.; Thouless, D.J. *The Quantum Hall Effect*; Springer: New York, NY, USA, 2012.
16. Laughlin, R.B. Quantized Hall conductivity in two dimensions. *Phys. Rev. B* **1981**, *23*, 5632. [[CrossRef](#)]
17. Thouless, D.J.; Kohmoto, M.; Nightingale, M.P.; Den, N.M.D. Quantized Hall conductance in a two-dimensional periodic potential. *Phys. Rev. Lett.* **1982**, *49*, 405. [[CrossRef](#)]
18. Haldane, F.D.M. Model for a quantum Hall effect without Landau levels: Condensed-matter realization of the “parity anomaly”. *Phys. Rev. Lett.* **1988**, *61*, 2015. [[CrossRef](#)] [[PubMed](#)]
19. Hatsugai, Y. Chern number and edge states in the integer quantum Hall effect. *Phys. Rev. Lett.* **1993**, *71*, 3697. [[CrossRef](#)]
20. Qi, X.; Hughes, T.L.; Zhang, S. Topological field theory of time-reversal invariant insulators. *Phys. Rev. B* **2008**, *78*, 195424. [[CrossRef](#)]
21. Haldane, F.D.M. Nobel lecture: Topological quantum matter. *Rev. Mod. Phys.* **2017**, *89*, 40502. [[CrossRef](#)]
22. Kane, C.L.; Mele, E.J. Z_2 topological order and the quantum spin Hall effect. *Phys. Rev. Lett.* **2005**, *95*, 146802. [[CrossRef](#)]
23. Bernevig, B.A.; Hughes, T.L.; Zhang, S.C. Quantum spin Hall effect and topological phase transition in HgTe quantum wells. *Science* **2006**, *314*, 1757. [[CrossRef](#)]
24. König, M.; Wiedmann, S.; Brüne, C.; Roth, A.; Buhmann, H.; Molenkamp, L.W.; Qi, D.L.; Zhang, S.C. Quantum spin Hall insulator state in HgTe quantum wells. *Science* **2007**, *318*, 766. [[CrossRef](#)]
25. Yu, R.; Zhang, W.; Zhang, H.J.; Zhang, S.C.; Dai, X.; Fang, Z. Quantized anomalous Hall effect in magnetic topological insulators. *Science* **2010**, *329*, 61. [[CrossRef](#)] [[PubMed](#)]
26. Chang, C.Z.; Zhang, J.; Feng, X.; Shen, J.; Zhang, Z.; Guo, M.; Li, K.; Ou, Y.; Wei, P.; Wang, L.L.; et al. Experimental observation of the quantum anomalous Hall effect in a magnetic topological insulator. *Science* **2013**, *340*, 167. [[CrossRef](#)] [[PubMed](#)]
27. Oh, S. The complete quantum Hall trio. *Science* **2013**, *340*, 153. [[CrossRef](#)]
28. Weng, H.; Yu, R.; Hu, X.; Dai, X.; Fang, Z. Quantum anomalous Hall effect and related topological electronic states. *Adv. Phys.* **2015**, *64*, 227. [[CrossRef](#)]
29. Fu, L.; Kane, C.L.; Mele, E.J. Topological insulators in three dimensions. *Phys. Rev. Lett.* **2007**, *98*, 106803. [[CrossRef](#)]
30. Fu, L.; Kane, C.L. Topological insulators with inversion symmetry. *Phys. Rev. B* **2007**, *76*, 45302. [[CrossRef](#)]
31. Hsieh, D.; Qian, D.; Wray, L.; Xia, Y.; Hor, Y.S.; Cava, R.J.; Hasan, M.Z. A topological Dirac insulator in a quantum spin Hall phase. *Nature* **2008**, *452*, 970. [[CrossRef](#)] [[PubMed](#)]
32. Neupane, M.; Richardella, A.; Sánchez-Barriga, J.; Xu, S.; Alidoust, N.; Belopolski, I.; Liu, C.; Bian, G.; Zhang, D.; Marchenko, D.; et al. Observation of quantum-tunnelling-modulated spin texture in ultrathin topological insulator Bi_2Se_3 films. *Nat. Commun.* **2014**, *5*, 3841. [[CrossRef](#)]
33. Xia, Y.; Qian, D.; Hsieh, D.; Wray, L.; Pal, A.; Lin, H.; Bansil, A.; Grauer, D.; Hor, Y.S.; Cava, R.J.; et al. Observation of a large-gap topological-insulator class with a single Dirac cone on the surface. *Nat. Phys.* **2009**, *5*, 398. [[CrossRef](#)]
34. Chen, E.J.; Analytis, J.G.; Chu, J.H.; Liu, Z.K.; Mo, S.K.; Qi, X.L.; Zhang, H.J.; Lu, D.H.; Dai, X.; Fang, Z.; et al. Experimental realization of a three-dimensional topological insulator, Bi_2Te_3 . *Science* **2009**, *325*, 178. [[CrossRef](#)] [[PubMed](#)]
35. Hsieh, D.; Xia, Y.; Qian, D.; Wray, L.; Meier, F.; Dil, J.H.; Osterwalder, J.; Patthey, L.; Fedorov, A.V.; Lin, H.; et al. Observation of time-reversal-protected single-Dirac-cone topological-insulator states in Bi_2Te_3 and Sb_2Te_3 . *Phys. Rev. Lett.* **2009**, *103*, 146401. [[CrossRef](#)] [[PubMed](#)]
36. Zhang, H.; Liu, C.X.; Qi, X.L.; Dai, X.; Fang, Z.; Zhang, S.C. Topological insulators in Bi_2Se_3 , Bi_2Te_3 and Sb_2Te_3 with a single Dirac cone on the surface. *Nat. Phys.* **2009**, *5*, 438. [[CrossRef](#)]
37. Roushan, P.; Seo, J.; Parker, C.; Hor, Y.S.; Hsieh, D.; Qian, D.; Richardella, A.; Hasan, M.Z.; Cava, R.J.; Yazdani, A. Topological surface states protected from backscattering by chiral spin texture. *Nature* **2009**, *460*, 1106–1109. [[CrossRef](#)]
38. Yang, Q.; Dolev, M.; Zhang, L.; Zhao, J.; Fried, A.D.; Schemm, E.; Liu, M.; Palevski, A.; Marshall, A.F.; Risbud, S.H.; et al. Emerging weak localization effects on a topological insulator–insulating ferromagnet (Bi_2Se_3 -EuS) interface. *Phys. Rev. B* **2013**, *88*, 081407. [[CrossRef](#)]
39. Arimoto, K.; Koretsune, T.; Nomura, K. Current-induced dynamics of isolated antiferromagnetic antiskyrmion and antiskyrmionium. *Phys. Rev. B* **2021**, *103*, 235315. [[CrossRef](#)]
40. Young, S.M.; Zaheer, S.; Teo, J.C.Y.; Kane, C.L.; Mele, E.J.; Rappe, A.M. Dirac semimetal in three dimensions. *Phys. Rev. Lett.* **2012**, *108*, 140405. [[CrossRef](#)]

41. Wang, Z.; Sun, Y.; Chen, X.Q.; Franchini, C.; Xu, G.; Weng, H.; Dai, X.; Fang, Z. Dirac semimetal and topological phase transitions in A_3Bi ($A=Na, K, Rb$). *Phys. Rev. B* **2012**, *85*, 195320. [[CrossRef](#)]
42. Wan, X.; Turner, A.M.; Vishwanath, A.; Savrasov, S.Y. Topological semimetal and fermi-arc surface states in the electronic structure of pyrochlore iridates. *Phys. Rev. B* **2011**, *83*, 205101. [[CrossRef](#)]
43. Weng, H.; Fang, C.; Fang, Z.; Bernevig, B.A.; Dai, X. Weyl semimetal phase in noncentrosymmetric transition-metal monophosphides. *Phys. Rev. X* **2015**, *5*, 11029. [[CrossRef](#)]
44. Lv, B.Q.; Weng, H.M.; Fu, B.B.; Wang, X.P.; Miao, H.; Ma, J.; Richard, P.; Huang, X.C.; Zhao, L.X.; Chen, G.F.; et al. Experimental discovery of Weyl semimetal TaAs. *Phys. Rev. X* **2015**, *5*, 31013. [[CrossRef](#)]
45. Liu, D.F.; Liang, A.J.; Liu, E.K.; Xu, Q.N.; Li, Y.W.; Chen, C.; Pei, D.; Shi, W.J.; Mo, S.K.; Dudin, P.; et al. Magnetic Weyl semimetal phase in a kagomé crystal. *Science* **2019**, *365*, 1282–1285. [[CrossRef](#)]
46. Wieder, B.J.; Kim, Y.; Rappe, A.M.; Kane, C.L. Double Dirac semimetals in three dimensions. *Phys. Rev. Lett.* **2016**, *116*, 186402. [[CrossRef](#)]
47. Liu, B.; Liu, Z.; Zhang, W.; Wang, Z.F. Symmetry-engineered nodal lines and hourglass fermions in patterned two-dimensional electron gas. *Phys. Rev. B* **2023**, *107*, 115423. [[CrossRef](#)]
48. Kim, Y.; Wieder, B.J.; Kane, C.L.; Rappe, A.M. Dirac line nodes in inversion-symmetric crystals. *Phys. Rev. Lett.* **2015**, *115*, 36806. [[CrossRef](#)]
49. Yu, R.; Weng, H.; Fang, Z.; Dai, X.; Hu, X. Topological node-line semimetal and Dirac semimetal state in antiperovskite Cu_3PdN . *Phys. Rev. Lett.* **2015**, *115*, 36807. [[CrossRef](#)] [[PubMed](#)]
50. Fang, C.; Weng, H.; Dai, X.; Fang, Z. Topological nodal line semimetals. *Chin. Phys. B* **2016**, *25*, 117106. [[CrossRef](#)]
51. Liu, Z.; Wang, H.; Wang, Z.F.; Yang, J.; Liu, F. Pressure-induced organic topological nodal-line semimetal in the three-dimensional molecular crystal $Pd(ddd)_2$. *Phys. Rev. B* **2018**, *97*, 155138. [[CrossRef](#)]
52. Wieder, B.J. Threes company. *Nat. Phys.* **2018**, *14*, 329–330. [[CrossRef](#)]
53. Bradlyn, B.; Cano, J.; Wang, Z.; Vergniory, M.G.; Felser, C.; Cava, R.J.; Bernevig, B.A. Beyond Dirac and Weyl fermions: Unconventional quasiparticles in conventional crystals. *Science* **2016**, *353*, 558. [[CrossRef](#)] [[PubMed](#)]
54. Jeon, S.; Zhou, B.B.; Gyenis, A.; Feldman, B.E.; Kimchi, I.; Potter, A.C.; Gibson, Q.D.; Cava, R.J.; Vishwanath, A.; Yazdani, A. Landau quantization and quasiparticle interference in the three-dimensional Dirac semimetal Cd_3As_2 . *Nat. Mater.* **2014**, *13*, 851–856. [[CrossRef](#)]
55. Feng, J.; Pang, Y.; Wu, D.; Wang, Z.; Weng, H.; Li, J.; Dai, X.; Fang, Z.; Shi, Y.; Lu, L. Large linear magnetoresistance in Dirac semimetal Cd_3As_2 with fermi surfaces close to the Dirac points. *Phys. Rev. B* **2015**, *92*, 081306. [[CrossRef](#)]
56. Zhang, C.L.; Xu, S.Y.; Belopolski, I.; Yuan, Z.; Lin, Z.; Tong, B.; Bian, G.; Alidoust, N.; Lee, C.C.; Huang, S.M.; et al. Signatures of the Adler–Bell–Jackiw chiral anomaly in a Weyl fermion semimetal. *Nat. Commun.* **2016**, *7*, 10735. [[CrossRef](#)] [[PubMed](#)]
57. Huang, X.; Zhao, L.; Long, Y.; Wang, P.; Chen, D.; Yang, Z.; Liang, H.; Xue, M.; Weng, H.; Fang, Z.; et al. Observation of the chiral-anomaly-induced negative magnetoresistance in 3D Weyl semimetal TaAs. *Phys. Rev. X* **2015**, *5*, 31023. [[CrossRef](#)]
58. Rajamathi, C.R.; Gupta, U.; Kumar, N.; Yang, H.; Sun, Y.; Süß, V.; Shekhar, C.; Schmidt, M.; Blumtritt, H.; Werner, P.; et al. Weyl semimetals as hydrogen evolution catalysts. *Adv. Mater.* **2017**, *29*, 1606202. [[CrossRef](#)]
59. Li, J.; Ma, H.; Xie, Q.; Feng, S.; Ullah, S.; Li, R.; Dong, J.; Li, D.; Li, Y.; Chen, X.Q. Topological quantum catalyst: Dirac nodal line states and a potential electrocatalyst of hydrogen evolution in the TiSi family. *Sci. China Mater.* **2018**, *61*, 23–29. [[CrossRef](#)]
60. Nayak, C.; Simon, S.H.; Stern, A.; Freedman, M.; Sarma, S.D. Non-Abelian anyons and topological quantum computation. *Rev. Mod. Phys.* **2008**, *80*, 1083. [[CrossRef](#)]
61. Yang, S.A. Dirac and Weyl materials: Fundamental aspects and some spintronics applications. *Spin* **2016**, *6*, 1640003. [[CrossRef](#)]
62. Novoselov, K.S.; Geim, A.K.; Morozov, S.V.; Jiang, D.; Zhang, Y.; Dubonos, S.V.; Grigorieva, I.V.; Firsov, A.A. Electric field effect in atomically thin carbon films. *Science* **2004**, *306*, 666. [[CrossRef](#)] [[PubMed](#)]
63. Zhang, Y.B.; Tan, Y.W.; Stormer, H.L.; Kim, P. Experimental observation of the quantum Hall effect and Berry’s phase in graphene. *Nature* **2005**, *438*, 201. [[CrossRef](#)] [[PubMed](#)]
64. Cao, Y.; Rodan-Legrain, D.; Rubies-Bigorda, O.; Park, J.M.; Watanabe, K.; Taniguchi, T.; Jarillo-Herrero, P. Tunable correlated states and spin-polarized phases in twisted bilayer-bilayer graphene. *Nature* **2020**, *583*, 215. [[CrossRef](#)]
65. Uri, A.; Grover, S.; Cao, Y.; Crosse, J.A.; Bagani, K.; Rodan-Legrain, D.; Myasoedov, Y.; Watanabe, K.; Taniguchi, T.; Moon, P.; et al. Mapping the twist-angle disorder and Landau levels in magic-angle graphene. *Nature* **2020**, *581*, 47. [[CrossRef](#)]
66. Liu, Z.K.; Zhou, B.; Zhang, Y.; Wang, Z.J.; Weng, H.M.; Prabhakaran, D.; Mo, S.K.; Shen, Z.X.; Fang, Z.; Dai, X.; et al. Discovery of a three-dimensional topological Dirac semimetal, Na_3Bi . *Science* **2014**, *343*, 864. [[CrossRef](#)]
67. Xu, S.Y.; Liu, C.; Kushwaha, S.K.; Sankar, R.; Krizan, J.W.; Belopolski, I.; Neupane, M.; Bian, G.; Alidoust, N.; Chang, T.R.; et al. Observation of fermi arc surface states in a topological metal. *Science* **2015**, *347*, 294. [[CrossRef](#)]
68. Xiong, J.; Kushwaha, S.K.; Liang, T.; Krizan, J.W.; Hirschberger, M.; Wang, W.D.; Cava, R.J.; Ong, N.P. Evidence for the chiral anomaly in the Dirac semimetal Na_3Bi . *Science* **2015**, *350*, 413. [[CrossRef](#)]
69. Xiong, J.; Kushwaha, S.; Krizan, J.; Liang, T.; Cava, R.J.; Ong, N.P. Anomalous conductivity tensor in the Dirac semimetal Na_3Bi . *Europhys. Lett.* **2016**, *114*, 27002. [[CrossRef](#)]
70. Wang, Z.J.; Weng, H.M.; Wu, Q.S.; Dai, X.; Fang, Z. Three-dimensional Dirac semimetal and quantum transport in Cd_3As_2 . *Phys. Rev. B* **2013**, *88*, 125427. [[CrossRef](#)]

71. Borisenko, S.; Gibson, Q.; Evtushinsky, D.; Zabolotnyy, V.; Büchner, B.; Cava, R.J. Experimental realization of a three-dimensional Dirac semimetal. *Phys. Rev. Lett.* **2014**, *113*, 27603. [[CrossRef](#)]
72. Liu, Z.K.; Jiang, J.; Zhou, B.; Wang, Z.J.; Zhang, Y.; Weng, H.M.; Prabhakaran, D.; Mo, S.K.; Peng, H.; Dudin, P.; et al. A stable three-dimensional topological Dirac semimetal Cd_3As_2 . *Nat. Mater.* **2014**, *13*, 677. [[CrossRef](#)]
73. Neupane, M.; Xu, S.Y.; Sankar, R.; Alidoust, N.; Bian, G.; Liu, C.; Belopolski, I.; Chang, T.R.; Jeng, H.T.; Lin, H.; et al. Observation of a three-dimensional topological Dirac semimetal phase in high-mobility Cd_3As_2 . *Nat. Commun.* **2014**, *5*, 3786. [[CrossRef](#)]
74. Liang, T.; Gibson, Q.; Ali, M.N.; Liu, M.H.; Cava, R.J.; Ong, N.P. Ultrahigh mobility and giant magnetoresistance in the Dirac semimetal Cd_3As_2 . *Nat. Mater.* **2015**, *14*, 280. [[CrossRef](#)]
75. Li, C.Z.; Wang, L.X.; Liu, H.W.; Wang, J.; Liao, Z.M.; Yu, D.P. Giant negative magnetoresistance induced by the chiral anomaly in individual Cd_3As_2 nanowires. *Nat. Commun.* **2015**, *6*, 10137. [[CrossRef](#)]
76. Li, H.; He, H.T.; Lu, H.Z.; Zhang, H.C.; Liu, H.C.; Ma, R.; Fan, Z.Y.; Shen, S.Q.; Wang, J.N. Negative magnetoresistance in Dirac semimetal Cd_3As_2 . *Nat. Commun.* **2016**, *7*, 10301. [[CrossRef](#)]
77. Wang, C.M.; Sun, H.P.; Lu, H.Z.; Xie, X.C. 3D quantum Hall effect of fermi arcs in topological semimetals. *Phys. Rev. Lett.* **2017**, *119*, 136806. [[CrossRef](#)] [[PubMed](#)]
78. Zhang, C.; Narayan, A.; Lu, S.H.; Zhang, J.L.; Zhang, H.Q.; Ni, Z.L.; Yuan, X.; Liu, Y.W.; Park, J.H.; Zhang, E.Z.; et al. Evolution of Weyl orbit and quantum Hall effect in Dirac semimetal Cd_3As_2 . *Nat. Commun.* **2017**, *8*, 1272. [[CrossRef](#)]
79. Huang, S.M.; Xu, S.Y.; Belopolski, I.; Lee, C.C.; Chang, G.Q.; Wang, B.K.; Alidoust, N.; Bian, G.; Neupane, M.; Zhang, C.L.; et al. A Weyl fermion semimetal with surface fermi arcs in the transition metal monopnictide TaAs class. *Nat. Commun.* **2015**, *6*, 7373. [[CrossRef](#)]
80. Lv, B.Q.; Xu, N.; Weng, H.M.; Ma, J.Z.; Richard, P.; Huang, X.C.; Zhao, L.X.; Chen, G.F.; Matt, C.E.; Bisti, F.; et al. Observation of Weyl nodes in TaAs. *Nat. Phys.* **2015**, *11*, 724. [[CrossRef](#)]
81. Xu, S.Y.; Belopolski, I.; Sanchez, D.S.; Zhang, C.L.; Chang, G.Q.; Guo, C.; Bian, G.; Yuan, Z.J.; Lu, H.; Chang, T.R.; et al. Experimental discovery of a topological Weyl semimetal state in TaP. *Sci. Adv.* **2015**, *1*, e1501092. [[CrossRef](#)]
82. Xu, S.Y.; Belopolski, I.; Alidoust, N.; Neupane, M.; Bian, G.; Zhang, C.L.; Sankar, R.; Chang, G.Q.; Yuan, Z.J.; Lee, C.C.; et al. Discovery of a Weyl fermion semimetal and topological fermi arcs. *Science* **2015**, *349*, 613. [[CrossRef](#)]
83. Xu, S.Y.; Alidoust, N.; Belopolski, I.; Yuan, Z.; Bian, G.; Chang, T.R.; Zheng, H.; Strocov, V.N.; Sanchez, D.S.; Chang, G. Discovery of a Weyl fermion state with fermi arcs in niobium arsenide. *Nat. Phys.* **2015**, *11*, 748. [[CrossRef](#)]
84. Liu, Z.K.; Yang, L.X.; Sun, Y.; Zhang, T.; Peng, H.; Yang, H.F.; Chen, C.; Zhang, Y.; Guo, Y.F.; Prabhakaran, D.; et al. Evolution of the fermi surface of Weyl semimetals in the transition metal pnictide family. *Nat. Mater.* **2016**, *15*, 27. [[CrossRef](#)]
85. Xu, N.; Weng, H.M.; Lv, B.Q.; Matt, C.E.; Park, J.; Bisti, F.; Strocov, V.N.; Gawryluk, D.; Pomjakushina, E.; Conder, K.; et al. Observation of Weyl nodes and fermi arcs in tantalum phosphide. *Nat. Commun.* **2016**, *7*, 11006. [[CrossRef](#)] [[PubMed](#)]
86. Arnold, F.; Shekhar, C.; Wu, S.C.; Sun, Y.; Dos Reis, R.D.; Kumar, N.; Naumann, M.; Ajeesh, M.O.; Schmidt, M.; Grushin, A.G.; et al. Negative magnetoresistance without well-defined chirality in the Weyl semimetal TaP. *Nat. Commun.* **2016**, *7*, 11615. [[CrossRef](#)]
87. Soluyanov, A.A.; Gresch, D.; Wang, Z.; Wu, Q.; Troyer, M.; Dai, X.; Bernevig, B.A. Type-II Weyl semimetals. *Nature* **2015**, *527*, 495. [[CrossRef](#)]
88. Wang, Z.; Gresch, D.; Soluyanov, A.A.; Xie, W.; Kushwaha, S.; Dai, X.; Troyer, M.; Cava, R.J.; Bernevig, B.A. MoTe_2 : A type-II Weyl topological metal. *Phys. Rev. Lett.* **2016**, *117*, 56805. [[CrossRef](#)] [[PubMed](#)]
89. Jiang, J.; Liu, Z.K.; Sun, Y.; Yang, H.F.; Rajamathi, C.R.; Qi, Y.P.; Yang, L.X.; Chen, C.; Peng, H.; Hwang, C.C.; et al. Signature of type-II Weyl semimetal phase in MoTe_2 . *Nat. Commun.* **2017**, *8*, 13973. [[CrossRef](#)]
90. Tamaï, A.; Wu, Q.S.; Cucchi, I.; Bruno, F.Y.; Riccò, S.; Kim, T.K.; Hoesch, M.; Barreateau, C.; Giannini, E.; Besnard, C.; et al. Fermi arcs and their topological character in the candidate type-II Weyl semimetal MoTe_2 . *Phys. Rev. X* **2016**, *6*, 31021.
91. Sun, Y.; Wu, S.C.; Ali, M.N.; Felser, C.; Yan, B.H. Prediction of Weyl semimetal in orthorhombic MoTe_2 . *Phys. Rev. B* **2015**, *92*, 161107. [[CrossRef](#)]
92. Deng, K.; Wan, G.L.; Deng, P.; Zhang, K.N.; Ding, S.J.; Wang, E.Y.; Yan, M.Z.; Huang, H.Q.; Zhang, H.Y.; Xu, Z.L.; et al. Experimental observation of topological fermi arcs in type-II Weyl semimetal MoTe_2 . *Nat. Phys.* **2016**, *12*, 1105. [[CrossRef](#)]
93. Autès, G.; Gresch, D.; Troyer, M.; Soluyanov, A.A.; Yazyev, O.V. Robust type-II Weyl semimetal phase in transition metal diphosphides XP_2 ($X=\text{Mo}, \text{W}$). *Phys. Rev. Lett.* **2016**, *117*, 66402. [[CrossRef](#)] [[PubMed](#)]
94. Koepf, K.; Kasinathan, D.; Efremov, D.V.; Khim, S.; Borisenko, S.; Büchner, B.; Van den Brink, J. TaIrTe_4 : A ternary type-II Weyl semimetal. *Phys. Rev. B* **2016**, *93*, 201101. [[CrossRef](#)]
95. Wu, Y.; Mou, D.; Jo, N.H.; Sun, K.; Huang, L.; Budko, S.L.; Canfield, P.C.; Kaminski, A. Observation of fermi arcs in the type-II Weyl semimetal candidate WTe_2 . *Phys. Rev. B* **2016**, *94*, 121113. [[CrossRef](#)]
96. Ali, M.N.; Xiong, J.; Flynn, S.; Tao, J.; Gibson, Q.D.; Schoop, L.M.; Liang, T.; Haldolaarachchige, N.; Hirschberger, M.; Ong, N.P.; et al. Large, non-saturating magnetoresistance in WTe_2 . *Nature* **2014**, *514*, 205. [[CrossRef](#)]
97. Li, P.; Wen, Y.; He, X.; Zhang, Q.; Xia, C.; Yu, Z.M.; Yang, S.A.; Zhu, Z.; Alshareef, H.N.; Zhang, X.X. Evidence for topological type-II Weyl semimetal WTe_2 . *Nat. Commun.* **2017**, *8*, 2150. [[CrossRef](#)] [[PubMed](#)]
98. Kang, D.F.; Zhou, Y.Z.; Yi, W.; Yang, C.L.; Guo, J.; Shi, Y.G.; Zhang, S.; Wang, Z.; Zhang, C.; Jiang, S.; et al. Superconductivity emerging from a suppressed large magnetoresistant state in tungsten ditelluride. *Nat. Commun.* **2015**, *6*, 7804. [[CrossRef](#)] [[PubMed](#)]
99. Burkov, A.A.; Hook, M.D.; Balents, L. Topological nodal semimetals. *Phys. Rev. B* **2011**, *84*, 235126. [[CrossRef](#)]

100. Hosen, M.M.; Dimitri, K.; Belopolski, I.; Maldonado, P.; Sankar, R.; Dhakal, N.; Dhakal, G.; Cole, T.; Oppeneer, P.M.; Kaczorowski, D.; et al. Tunability of the topological nodal-line semimetal phase in ZrSiX-type materials (X=S, Se, Te). *Phys. Rev. B* **2017**, *95*, 161101. [[CrossRef](#)]
101. Neupane, M.; Belopolski, I.; Hosen, M.M.; Sanchez, D.S.; Sankar, R.; Szlowska, M.; Xu, S.Y.; Dimitri, K.; Dhakal, N.; Maldonado, P.; et al. Observation of topological nodal fermion semimetal phase in ZrSiS. *Phys. Rev. B* **2016**, *93*, 201104. [[CrossRef](#)]
102. Schoop, L.M.; Ali, M.N.; Straßer, C.; Topp, A.; Varykhalov, A.; Marchenko, D.; Duppel, V.; Parkin, S.S.P.; Lotsch, B.V.; Ast, C.R. Dirac cone protected by non-symmorphic symmetry and three-dimensional Dirac line node in ZrSiS. *Nat. Commun.* **2016**, *7*, 11696. [[CrossRef](#)]
103. Hu, J.; Tang, Z.J.; Liu, J.Y.; Liu, X.; Zhu, Y.L.; Graf, D.; Myhro, K.; Tran, S.; Lau, C.N.; Wei, J.; et al. Evidence of topological nodal-line fermions in ZrSiSe and ZrSiTe. *Phys. Rev. Lett.* **2016**, *117*, 16602. [[CrossRef](#)]
104. Takane, D.; Wang, Z.; Souma, S.; Nakayama, K.; Trang, C.X.; Sato, T.; Takahashi, T.; Ando, Y. Dirac-node arc in the topological line-node semimetal HfSiS. *Phys. Rev. B* **2016**, *94*, 121108. [[CrossRef](#)]
105. Bian, G.; Chang, T.R.; Sankar, R.; Xu, S.Y.; Zheng, H.; Neupert, T.; Chiu, C.K.; Huang, S.M.; Chang, G.; Belopolski, I.; et al. Topological nodal-line fermions in spin-orbit metal PbTaSe₂. *Nat. Commun.* **2016**, *7*, 10556. [[CrossRef](#)]
106. Yang, S.Y.; Yang, H.; Derunova, E.; Parkin, S.S.P.; Yan, B.H.; Ali, M.N. Symmetry demanded topological nodal-line materials. *Adv. Phys.-X* **2018**, *3*, 1414631. [[CrossRef](#)]
107. Kitaev, A. Periodic table for topological insulators and superconductors. *AIP Conf. Proc.* **2009**, *1134*, 22–30.
108. Stone, M.; Chiu, C.K.; Roy, A. Symmetries, dimensions and topological insulators: The mechanism behind the face of the Bott clock. *J. Phys. A: Math. Theor.* **2010**, *44*, 45001. [[CrossRef](#)]
109. Chiu, C.K.; Teo, J.C.Y.; Schnyder, A.P.; Ryu, S. Classification of topological quantum matter with symmetries. *Rev. Mod. Phys.* **2016**, *88*, 35005. [[CrossRef](#)]
110. Fu, L. Topological crystalline insulators. *Phys. Rev. Lett.* **2011**, *106*, 106802. [[CrossRef](#)] [[PubMed](#)]
111. Hsieh, T.; Lin, H.; Liu, J.; Duan, W.; Bansil, A.; Fu, L. Topological crystalline insulators in the SnTe material class. *Nat. Commun.* **2012**, *3*, 982. [[CrossRef](#)]
112. Tanaka, Y.; Ren, Z.; Sato, T.; Nakayama, K.; Souma, S.; Takahashi, T.; Kouji, S.; Yoichi, A. Experimental realization of a topological crystalline insulator in SnTe. *Nat. Phys.* **2012**, *8*, 800–803.
113. Dziawa, P.; Kowalski, B.; Dybko, K.; Buczko, R.; Szczerbakow, A.; Szot, M.; Lusakowska, E.; Balasubramanian, T.; Wojek, B.M.; Berntsen, M.H.; et al. Topological crystalline insulator states in Pb_{1-x}Sn_xSe. *Nat. Mater.* **2012**, *11*, 1023–1027. [[PubMed](#)]
114. Wang, Z.; Alexandradinata, A.; Cava, R.J.; Bernevig, B.A. Hourglass fermions. *Nature* **2016**, *532*, 189–194. [[PubMed](#)]
115. Ma, J.; Yi, C.; Lv, B.; Wang, Z.; Nie, S.; Wang, L.; Kong, L.; Huang, Y.; Richard, P.; Zhang, P.; et al. Experimental evidence of hourglass fermion in the candidate nonsymmorphic topological insulator KHgSb. *Sci. Adv.* **2017**, *3*, e1602415.
116. Liu, C.X.; Zhang, R.X.; VanLeeuwen, B.K. Topological nonsymmorphic crystalline insulators. *Phys. Rev. B* **2014**, *90*, 85304.
117. Fang, C.; Fu, L. New classes of three-dimensional topological crystalline insulators: Nonsymmorphic and magnetic. *Phys. Rev. B* **2015**, *91*, 161105.
118. Shiozaki, K.; Sato, M.; Gomi, K. Z₂ topology in nonsymmorphic crystalline insulators: Möbius twist in surface states. *Phys. Rev. B* **2015**, *91*, 155120. [[CrossRef](#)]
119. Fang, C.; Fu, L. New classes of topological crystalline insulators having surface rotation anomaly. *Sci. Adv.* **2019**, *5*, eaat2374.
120. Zhang, T.; Yue, C.; Zhang, T.; Nie, S.; Wang, Z.; Fang, C.; Weng, H.; Fang, Z. Topological crystalline insulators with C₂ rotation anomaly. *Phys. Rev. Res.* **2019**, *1*, 12001.
121. Bradlyn, B.; Elcoro, L.; Cano, J.; Vergniory, M.G.; Wang, Z.; Felser, C.; Aroyo, M.I.; Bernevig, B.A. Topological quantum chemistry. *Nature* **2017**, *547*, 298–305.
122. Po, H.C.; Vishwanath, A.; Watanabe, H. Symmetry-based indicators of band topology in the 230 space groups. *Nat. Commun.* **2017**, *8*, 50. [[PubMed](#)]
123. Zhang, T.; Jiang, Y.; Song, Z.; Huang, H.; He, Y.; Fang, Z.; Weng, H.; Fang, C. Catalogue of topological electronic materials. *Nature* **2019**, *566*, 475–479.
124. Silveirinha, M.G. Proof of the bulk-edge correspondence through a link between topological photonics and fluctuation-electrodynamics. *Phys. Rev. X* **2019**, *9*, 11037.
125. Parameswaransa, S.A.; Wan, Y. Topological insulators turn a corner. *Physics* **2017**, *10*, 132. [[CrossRef](#)]
126. Schindler, F.; Cook, A.M.; Vergniory, M.G.; Wang, Z.; Parkin, S.S.P.; Bernevig, B.A.; Neupert, T. Higher-order topological insulators. *Sci. Adv.* **2018**, *4*, eaat0346.
127. Serra-Garcia, M.; Peri, V.; Süsstrunk, R.; Bilal, O.R.; Larsen, T.; Villanueva, L.G.; Huber, S.D. Observation of a phononic quadrupole topological insulator. *Nature* **2018**, *555*, 342–345. [[PubMed](#)]
128. Peterson, C.W.; Benalcazar, W.A.; Hughes, T.L.; Bahl, G. A quantized microwave quadrupole insulator with topologically protected corner states. *Nature* **2018**, *555*, 346–350. [[PubMed](#)]
129. Imhof, S.; Berger, C.; Bayer, F.; Brehm, J.; Molenkamp, L.W.; Kiessling, T.; Schindler, F.; Lee, C.H.; Greiter, M.; Neupert, T.; et al. Topoelectrical-circuit realization of topological corner modes. *Nat. Phys.* **2018**, *14*, 925–929.
130. Xue, H.R.; Yang, Y.H.; Gao, F.; Chong, Y.; Zhang, B. Acoustic higher-order topological insulator on a kagome lattice. *Nat. Mater.* **2019**, *18*, 108–112.

131. Ni, X.; Weiner, M.; Alu, A.; Khanikaev, A.B. Observation of higher-order topological acoustic states protected by generalized chiral symmetry. *Nat. Mater.* **2019**, *18*, 113–120.
132. Noh, J.; Benalcazar, W.A.; Huang, S.; Collins, M.J.; Chen, K.P.; Hughes, T.L.; Rechtsman, M.C. Topological protection of photonic mid-gap defect modes. *Nat. Photonics* **2018**, *12*, 408–415.
133. Fan, H.; Xia, B.; Tong, L.; Zheng, S.; Yu, D. Elastic higher-order topological insulator with topologically protected corner states. *Phys. Rev. Lett.* **2019**, *122*, 204301. [[CrossRef](#)] [[PubMed](#)]
134. Benalcazar, W.A.; Bernevig, B.A.; Hughes, T.L. Quantized electric multipole insulators. *Science* **2017**, *357*, 61–66.
135. Benalcazar, W.A.; Bernevig, B.A.; Hughes, T.L. Electric multipole moments, topological multipole moment pumping, and chiral hinge states in crystalline insulators. *Phys. Rev. B* **2017**, *96*, 245115.
136. Raab, R.E.; De Lange, O.L. *Multipole Theory in Electromagnetism: Classical, Quantum, and Symmetry Aspects, with Applications*; OUP: Oxford, UK, 2004.
137. Mittal, S.; Orre, V.V.; Zhu, G.Y.; Gorlach, M.A.; Poddubny, A.; Hafezi, M. Photonic quadrupole topological phases. *Nat. Photonics* **2019**, *13*, 692–696.
138. He, L.; Addison, Z.; Mele, E.J.; Zhen, B. Quadrupole topological photonic crystals. *Nat. Commun.* **2020**, *11*, 3119. [[PubMed](#)]
139. Zhou, X.X.; Lin, Z.K.; Lu, W.X.; Lai, Y.; Hou, B.; Jiang, J.H. Twisted quadrupole topological photonic crystals. *Laser Photon. Rev.* **2020**, *14*, 2000010. [[CrossRef](#)]
140. Su, W.P.; Schrieffer, J.R.; Heeger, A.J. Solitons in polyacetylene. *Phys. Rev. Lett.* **1979**, *42*, 1698–1701.
141. Liu, F.; Wakabayashi, K. Novel topological phase with a zero berry curvature. *Phys. Rev. Lett.* **2017**, *118*, 76803.
142. Ezawa, M. Higher-order topological insulators and semimetals on the breathing kagome and pyrochlore lattices. *Phys. Rev. Lett.* **2018**, *120*, 026801.
143. Xie, B.Y.; Wang, H.F.; Wang, H.X.; Zhu, X.Y.; Jiang, J.H.; Lu, M.H.; Chen, Y.F. Second-order photonic topological insulator with corner states. *Phys. Rev. B* **2018**, *98*, 205147. [[CrossRef](#)]
144. Chen, X.D.; Deng, W.M.; Shi, F.L.; Zhao, F.L.; Chen, M.; Dong, J.W. Direct observation of corner states in second-order topological photonic crystal slabs. *Phys. Rev. Lett.* **2019**, *122*, 233902. [[CrossRef](#)]
145. Xie, B.Y.; Su, G.X.; Wang, H.F.; Su, H.; Shen, X.P.; Zhan, P.; Lu, M.H.; Wang, Z.L.; Chen, Y.F. Visualization of higher-order topological insulating phases in two-dimensional dielectric photonic crystals. *Phys. Rev. Lett.* **2019**, *122*, 233903. [[CrossRef](#)]
146. Benalcazar, W.A.; Li, T.H.; Hughes, T.L. Quantization of fractional corner charge in C_n -symmetric higher-order topological crystalline insulators. *Phys. Rev. B* **2019**, *99*, 245151. [[CrossRef](#)]
147. Li, M.Y.; Zhirihin, D.; Gorlach, M.; Ni, X.; Filonov, D.; Slobzhanyuk, A.; Alù, A.; Khanikaev, A.B. Higher-order topological states in photonic kagome crystals with longrange interactions. *Nat. Photonics* **2020**, *14*, 89–94. [[CrossRef](#)]
148. El Hassan, A.; Kunst, F.K.; Moritz, A.; Andler, G.; Bergholtz, E.J.; Bourennane, M. Corner states of light in photonic waveguides. *Nat. Photonics* **2019**, *13*, 697–700. [[CrossRef](#)]
149. Langbehn, J.; Peng, Y.; Trifunovic, L.; Oppen, F.; Brouwer, P.W. Reflection-symmetric second-order topological insulators and superconductors. *Phys. Rev. Lett.* **2017**, *119*, 246401. [[CrossRef](#)]
150. Schindler, F.; Wang, Z.; Vergniory, M.G.; Cook, A.M.; Murani, A.; Sengupta, S.; Kasumov, A.Y.; Deblock, R.; Jeon, S.; Drozdov, I.; et al. Higher-order topology in bismuth. *Nat. Phys.* **2018**, *14*, 918–924. [[CrossRef](#)]
151. Wang, Z.; Wieder, B.J.; Li, J.; Yan, B.; Bernevig, B.A. Higher-order topology, monopole nodal lines, and the origin of large fermi arcs in transition metal dichalcogenides XTe_2 ($X = Mo, W$). *Phys. Rev. Lett.* **2019**, *123*, 186401. [[CrossRef](#)] [[PubMed](#)]
152. Yue, C.; Xu, Y.; Song, Z.; Weng, H.; Lu, Y.M.; Fang, C.; Dai, X. Symmetry-enforced chiral hinge states and surface quantum anomalous Hall effect in the magnetic axion insulator $Bi_{2-x}Sm_xSe_3$. *Nat. Phys.* **2019**, *15*, 577–581. [[CrossRef](#)]
153. Xu, Y.; Song, Z.; Wang, Z.; Weng, H.; Dai, X. Higher-order topology of the axion insulator $EuIn_2As_2$. *Phys. Rev. Lett.* **2019**, *122*, 256402. [[CrossRef](#)]
154. Park, M.J.; Kim, Y.; Cho, G.Y.; Li, S. Higher-order topological insulator in twisted bilayer graphene. *Phys. Rev. Lett.* **2019**, *123*, 216803.
155. Liu, B.; Xian, L.; Mu, H.; Zhao, G.; Liu, Z.; Rubio, A.; Wang, Z.F. Higher-order band topology in twisted Moiré superlattice. *Phys. Rev. Lett.* **2021**, *126*, 66401. [[CrossRef](#)]
156. Sheng, X.L.; Chen, C.; Liu, H.; Chen, Z.; Yu, Z.M.; Zhao, Y.X.; Yang, S.A. Two-dimensional second-order topological insulator in graphdiyne. *Phys. Rev. Lett.* **2019**, *123*, 256402. [[CrossRef](#)]
157. Lee, E.; Kim, R.; Ahn, J.; Yang, B.J. Two-dimensional higher-order topology in monolayer graphdiyne. *npj Quantum Mater.* **2020**, *5*, 1.
158. Mu, H.; Liu, B.; Hu, T.; Wang, Z.F. Kekule lattice in graphdiyne: Coexistence of phononic and electronic second-order topological insulator. *Nano Lett.* **2022**, *22*, 1122–1128. [[CrossRef](#)]
159. Liu, B.; Zhao, G.; Liu, Z.; Wang, Z.F. Two-dimensional quadrupole topological insulator in γ -graphyne. *Nano Lett.* **2019**, *19*, 6492–6497. [[CrossRef](#)] [[PubMed](#)]
160. Mu, H.; Zhao, G.; Zhang, H.; Wang, Z.F. Antiferromagnetic second-order topological insulator with fractional mass-kink. *npj Comput. Mater.* **2022**, *8*, 82.
161. Hu, T.; Zhang, T.; Mu, H.; Wang, Z.F. Intrinsic second-order topological insulator in two-dimensional covalent organic frameworks. *J. Phys. Chem. Lett.* **2022**, *13*, 10905–10911. [[CrossRef](#)] [[PubMed](#)]

162. Xie, X.; Zhang, W.X.; He, X.W.; Wu, S.; Dang, J.; Peng, K.; Song, F.; Yang, L.; Ni, H.; Niu, Z.; et al. Cavity quantum electrodynamics with second-order topological corner state. *Laser Photon. Rev.* **2020**, *14*, 1900425. [[CrossRef](#)]
163. Zhang, W.X.; Xie, X.; Hao, H.M.; Dang, J.; Xiao, S.; Shi, S.; Ni, H.; Niu, Z.; Wang, C.; Jin, K.; et al. Low-threshold topological nanolasers based on the second-order corner state. *Light Sci Appl* **2020**, *9*, 109. [[CrossRef](#)]
164. Zhang, L.; Yang, Y.H.; Lin, Z.K.; Qin, P.; Chen, Q.; Gao, F.; Li, E.; Jiang, J.H.; Zhang, B.; Chen, H. Higher-order topological states in surface-wave photonic crystals. *Adv. Sci.* **2020**, *7*, 1902724. [[CrossRef](#)]
165. Luo, X.W.; Zhang, C.W. Higher-order topological corner states induced by gain and loss. *Phys. Rev. Lett.* **2019**, *123*, 73601. [[CrossRef](#)]
166. Liu, T.; Zhang, Y.R.; Ai, Q.; Gong, Z.; Kawabata, K.; Ueda, M.; Nori, F. Second-order topological phases in non-Hermitian systems. *Phys. Rev. Lett.* **2019**, *122*, 76801. [[CrossRef](#)] [[PubMed](#)]
167. Ezawa, M. Magnetic second-order topological insulators and semimetals. *Phys. Rev. B* **2018**, *97*, 155305. [[CrossRef](#)]
168. Wei, Q.; Zhang, X.; Deng, W.; Lu, J.; Huang, X.; Yan, M.; Chen, G.; Liu, Z.; Jia, S. Higher-order topological semimetal in acoustic crystals. *Nat. Mater.* **2021**, *20*, 812–817.
169. Wang, H.X.; Lin, Z.K.; Jiang, B.; Guo, G.Y.; Jiang, J.H. Higher-order Weyl semimetals. *Phys. Rev. Lett.* **2020**, *125*, 146401. [[CrossRef](#)]
170. Luo, L.; Wang, H.X.; Lin, Z.K.; Jiang, B.; Wu, Y.; Li, F.; Jiang, J.H. Observation of a phononic higher-order Weyl semimetal. *Nat. Mater.* **2021**, *20*, 794–799. [[CrossRef](#)]
171. Wang, Z.; Liu, D.; Teo, H.T.; Xue, H.; Zhang, B. Higher-order Dirac semimetal in a photonic crystal. *Phys. Rev. B* **2022**, *105*, L060101. [[CrossRef](#)]
172. Lin, M.; Hughes, T.L. Topological quadrupolar semimetals. *Phys. Rev. B* **2018**, *98*, 241103. [[CrossRef](#)]
173. Ghorashi, S.A.A.; Li, T.; Hughes, T.L. Higher-order Weyl semimetals. *Phys. Rev. Lett.* **2020**, *125*, 266804. [[CrossRef](#)]
174. Chen, C.; Zeng, X.T.; Chen, Z.; Zhao, Y.X.; Sheng, X.L.; Yang, S.A. Second-order real nodal-line semimetal in three-dimensional graphdiyne. *Phys. Rev. Lett.* **2022**, *128*, 26405. [[CrossRef](#)]
175. Zhang, Y.; Tang, J.; Dai, X.; Zhang, S.; Cao, Z.; Xiang, Y. Design of a higher-order nodal-line semimetal in a spring-shaped acoustic topological crystal. *Phys. Rev. B* **2022**, *106*, 184101. [[CrossRef](#)]
176. Wang, K.; Dai, J.X.; Shao, L.B.; Yang, S.A.; Zhao, Y.X. Boundary criticality of PT-invariant topology and second-order nodal-line semimetals. *Phys. Rev. Lett.* **2020**, *125*, 126403. [[CrossRef](#)]
177. Zhao, Y.X.; Lu, Y. PT-symmetric real Dirac fermions and semimetals. *Phys. Rev. Lett.* **2017**, *118*, 56401. [[CrossRef](#)]
178. Ahn, J.; Park, S.; Kim, D.; Kim, Y.; Yang, B.J. Stiefel–Whitney classes and topological phases in band theory. *Chin. Phys. B* **2019**, *28*, 117101. [[CrossRef](#)]
179. Ahn, J.; Kim, D.; Kim, Y.; Yang, B.J. Band topology and linking structure of nodal line semimetals with Z_2 monopole charges. *Phys. Rev. Lett.* **2018**, *121*, 106403. [[CrossRef](#)]
180. Fang, C.; Chen, Y.; Kee, H.Y.; Fu, L. Topological nodal line semimetals with and without spin-orbital coupling. *Phys. Rev. B* **2015**, *92*, 081201. [[CrossRef](#)]
181. Liu, F.; Deng, H.Y.; Wakabayashi, K. Helical topological edge states in a quadrupole phase. *Phys. Rev. Lett.* **2019**, *122*, 86804. [[CrossRef](#)]
182. Hsu, C.H.; Zhou, X.; Chang, T.R.; Ma, Q.; Gedik, N.; Bansil, A.; Xu, S.Y.; Lin, H.; Fu, L. Topology on a new facet of bismuth. *Proc. Natl. Acad. Sci. USA* **2019**, *116*, 13255. [[CrossRef](#)]
183. Choi, Y.B.; Xie, Y.; Chen, C.Z.; Park, J.; Song, S.B.; Yoon, J.; Kim, B.J.; Taniguchi, T.; Watanabe, K.; Kim, J.; et al. Evidence of higher-order topology in multilayer WTe_2 from Josephson coupling through anisotropic hinge states. *Nat. Mater.* **2020**, *19*, 974. [[CrossRef](#)] [[PubMed](#)]
184. Noguchi, R.; Kobayashi, M.; Jiang, Z.; Kuroda, K.; Takahashi, T.; Xu, Z.; Lee, D.; Hirayama, M.; Ochi, M.; Shirasawa, T.; et al. Evidence for a higher-order topological insulator in a three-dimensional material built from van der Waals stacking of bismuth-halide chains. *Nat. Mater.* **2021**, *20*, 473. [[CrossRef](#)] [[PubMed](#)]
185. Ezawa, M. Topological switch between second-order topological insulators and topological crystalline insulators. *Phys. Rev. Lett.* **2018**, *121*, 116801. [[CrossRef](#)]
186. Ren, Y.; Qiao, Z.; Niu, Q. Engineering corner states from two-dimensional topological insulators. *Phys. Rev. Lett.* **2020**, *124*, 166804. [[CrossRef](#)] [[PubMed](#)]
187. Chen, C.; Song, Z.; Zhao, J.Z.; Chen, Z.; Yu, Z.M.; Sheng, X.L.; Yang, S.A. Universal approach to magnetic second-order topological insulator. *Phys. Rev. Lett.* **2020**, *125*, 56402. [[CrossRef](#)]
188. Zhang, R.X.; Wu, F.; Das, S.S. Möbius insulator and higher-order topology in $MnBi_{2n}Te_{3n+1}$. *Phys. Rev. Lett.* **2020**, *124*, 136407. [[CrossRef](#)]
189. Huang, H.Q.; Liu, F. Structural buckling induced higher-order topology. *Natl. Sci. Rev.* **2021**, *9*, nwab170. [[CrossRef](#)]
190. Ezawa, M. Strong and weak second-order topological insulators with hexagonal symmetry and Z_3 index. *Phys. Rev. B* **2018**, *97*, 241402. [[CrossRef](#)]
191. Liu, J.W.; Hsieh, T.H.; Wei, P.; Duan, W.H.; Moodera, J.; Fu, L. Spin-filtered edge states with an electrically tunable gap in a two-dimensional topological crystalline insulator. *Nat. Mater.* **2014**, *13*, 178–183. [[CrossRef](#)]

192. Zeng, Y.J.; Feng, Y.X.; Tang, L.M.; Chen, K.Q. Effect of out-of-plane strain on the phonon structures and anharmonicity of twisted multilayer graphene. *Appl. Phys. Lett.* **2021**, *118*, 183103. [[CrossRef](#)]
193. Jiang, J.W.; Park, H.S. Strain tunable phononic topological bandgaps in two-dimensional hexagonal boron nitride. *J. Appl. Phys.* **2019**, *125*, 82511. [[CrossRef](#)]

Disclaimer/Publisher's Note: The statements, opinions and data contained in all publications are solely those of the individual author(s) and contributor(s) and not of MDPI and/or the editor(s). MDPI and/or the editor(s) disclaim responsibility for any injury to people or property resulting from any ideas, methods, instructions or products referred to in the content.